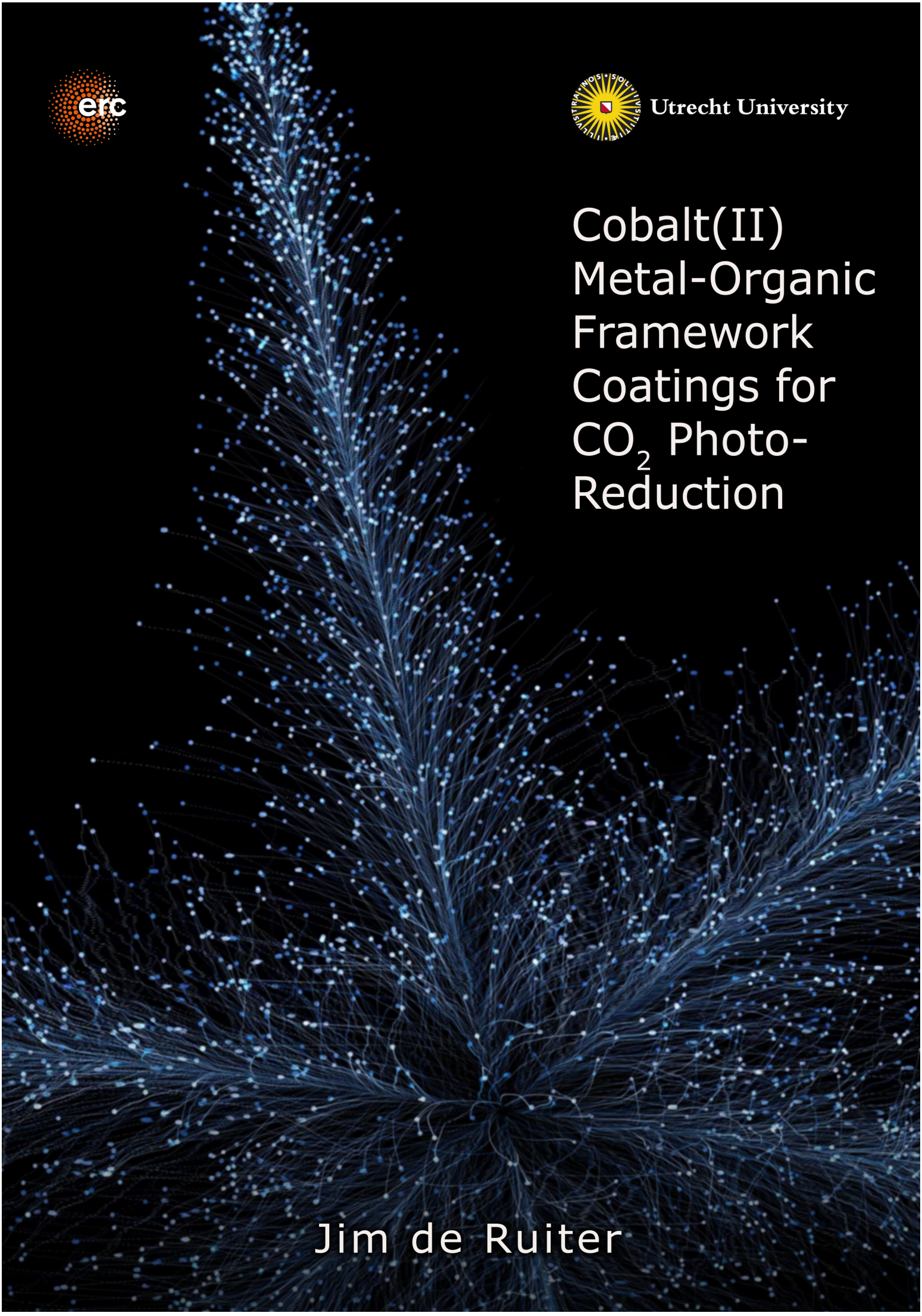

Utrecht University

Cobalt(II) Metal-Organic Framework Coatings for CO_2 Photo-Reduction

Jim de Ruiter

Master Thesis

Cobalt(II) Metal-Organic Framework Coatings for CO_2 Photo-Reduction.

Author:
Jim de Ruiter

Supervisors:
Guusje Delen, MSc
Dr. Florian Meirer
Prof. dr. ir. Bert M. Weckhuysen

February 20, 2019

Utrecht University
Debye Institute for Nanomaterials Science
Inorganic Chemistry and Catalysis

Abstract

This thesis describes synthesis, analysis, photo- and electro-catalytic experiments of cobalt(II) based metal organic framework (MOF) thin films. Organic molecules 4,4'-bipyridine (44BP), 2,4-dihydroxy terephthalic acid (DHTA) and amino terephthalic acid (ATA) were used as linkers. MOFs thin films were prepared on an acid or amine functionalized gold substrate or FTO glass. Homogeneous films of Co44BP were prepared using a layer-by-layer synthesis approach. The coordination of 44BP to the cobalt was observed with IR and Raman measurements. Identical crystalline thin films of Co44BP anchored on acid, hydroxide and pyridine terminated surfaces were revealed by XRD measurements. Homogeneous distributed Co44BP crystals over the surfaces were confirmed with Time of Flight Secondary Ion Mass Spectrometry (ToFSIMS) measurements. Thin films of CoDHTA and CoATA were prepared by spin coating. Vibrational analysis with IR and Raman, and DFT calculations showed that not only the acid groups, but the substituents, -OH and -NH_2, were also involved in the coordination. Combined with XRD analysis, the synthesis of the thin films resulted in poly crystalline CoDHTA and amorphous CoATA coatings. XRD measurements and Photo induced Force Microscopy (PiFM) on the CoDHTA thin films indicated that the crystalline orientation of CoDHTA differed on acid terminated surfaces compared to hydroxide terminated surfaces. For CoATA thin films, these measurements revealed very homogeneous amorphous films in both spatial and chemical perspectives. Ligand to metal charge transfer (LMCT) energies of CoDHTA and CoATA were observed at 382 nm and 375 nm respectively. Transients were observed with transient absorption spectroscopy (TAS) in CoDHTA and Co44BP with half-lifes up to respectively 139 and 141 ns. Activity in the catalytic testing of CoDHTA@FTO on the photoreduction of CO_2 and electrochemical reduction of methylene blue were barely observed. During the electrocatalysis, the coating was destroyed.

Contents

Introduction

Metal organic frameworks (MOFs) are materials made from metal nodes that are coordinated to organic linkers, Figure 1.1a [1, 2]. The organic linkers typically contain two or more functional groups such as acid, hydroxide or immidazole groups. The metals can coordinate to such groups and by alternately doing this, a network of metal-organic coordination units arises creating 2D or 3D structures. The construction of the framework in MOFs results in empty spaces within the coordination network which makes MOFs porous materials. The various kinds of metals and organic linkers that can be used makes MOFs highly tunable. By playing with different metals and organic linkers, various types of MOFs can be prepared to be used in applications such as gas separation and storage [3], (optical) sensors [4] and catalysis [2, 5]. For the last decades, research on MOFs thin films has gained more attention. Compared to bulk powder, thin films have more potential in industrial applications such as in electronic devices or functional coatings [6–8]. These functional coatings could be a promising tool for catalytic purposes especially in photo-catalysis. MOFs not only have a structural tunability, they also have an optical tunability. Both the organic linkers and metal ions can be used for light harvesting and combined with the fact that they are highly porous materials make them promising candidates as photo-catalysts. In this thesis, the synthesis of MOF thin films for the photo-reduction of CO_2 is described. CO_2 is a product that is mainly caused by the burning of fossil fuels. The CO_2 can be collected and converted into usable compounds such as the chemical building blocks CO and methanol [9]. Using sunlight as a carbon-neutral energy source helps to create a more sustainable world [10].
Cobalt(II) as metal ion in MOFs can be promising for the photoreduction of CO_2 as it has already shown promising results [11, 12]. In this thesis, the organic molecules amino-terephthalic acid (ATA) and 2,4-dihydroxy terephthalic acid (DHTA) were used as organic linkers, Figure 1.1. These terephthalic acid derivatives contain respectively amino and hydroxy groups. These groups have lone pairs that act as an 'antenna' and stimulate the collection of light. Various studies on the (photo)-catalytic potential of these organic linkers have already been performed. In the paper of Lee *et al.*, for example, MOFs with Zr and Ti were prepared with ATA for the photo-reduction of CO_2 [13]. Palomino Cabello *et al.* described various MOF structures with DHTA and different metals [14]. Furthermore, 4,4'-bipyridine (44BP) is used as organic linker as well, Figure 1.1. 44BP has a promising conjugated π structure that can be interesting for electron transport. In the following chapters the observations, difficulties and complexity among the syntheses of cobalt(II) 44BP (Co44BP), cobalt(II) DHTA (CoDHTA) and cobalt(II) ATA (CoATA) are extensively discussed. The light harvesting performance of these materials was studied and the first results on the catalytic activity is presented.

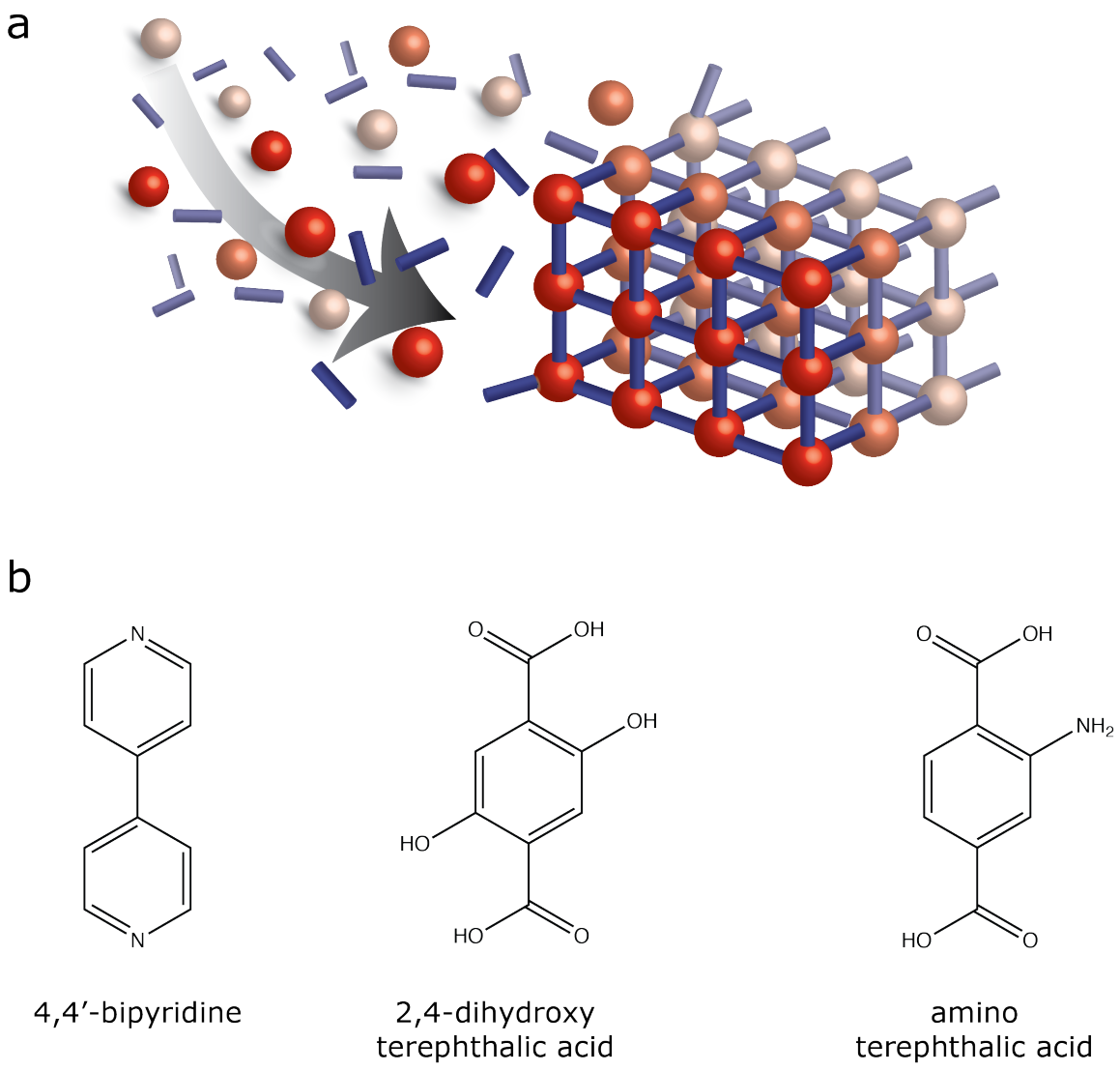

Figure 1.1: a: Illustration of a Metal-Organic Framework. This material is constructed out of organic molecules coordinated to metal ions. b: Structures of the organic linkers that have been used in the synthesis of the cobalt(II) MOF thin films

Theory

2.1 Theoretical background of MOFs and MOF thin films

In the early stages of coordination polymers, simple coordination networks were found. For example a network of Cu^{+} ions with a nitril based linker. In these networks, the node of the MOF is only the metal. The bond strength of these coordinations is however frial and the framework lacks architectural stability. In 1998, MOF-2 was prepared with $Zn_2{}^{+}$ ions and 1,4-benzene dicarboxylate. The coordination network of this MOF is not based on a single metal ion node, but consists of dinuclear zinc paddle wheel clusters. In general such metal clusters are referred to as secondary building units (SBUs). The structure of the SBUs depend on the metal ions and the interaction with the organic linker. MOFs that consists of SBUs are thermodynamic more stable because they consist of strong bonds such as metal-oxygen, C-O and C-C bond. [15]. The formation of SBUs forms the structural basis of many MOFs and by using different organic linkers and metal ions, various MOF structures can be prepared as bulk powder or thin film [1].
Metal-Organic Framework thin films, or often referred to as surface-anchored films of Metal-Organic Frameworks (SURMOFs) can roughly be classified in three groups. First, there are (mono)crystalline MOF films, Figure 2.2a. Ideally these thin films have large in-plane single-crystal domains. The roughness of these homogeneous films is typical not more than a few crystal building cells (a few nano-meters). Subsequently to this there are poly crystalline MOF films. These films do not have single-crystalline domains but consists of multiple oriented crystals anchored on the surface, Figure 2.2b [7]. Finally, amorphous MOF films can be prepared. In these films, the metal ion and organic linker are coordinated but do not form a crystalline network, but an amorous phase, Figure 2.2c [16].

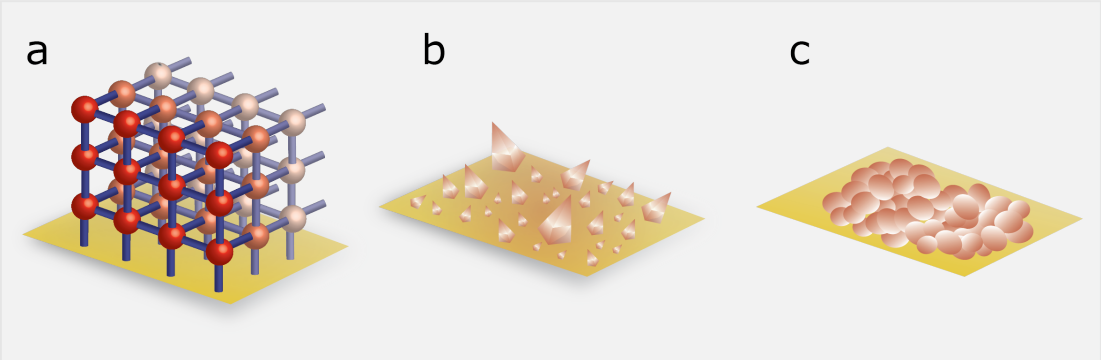

Figure 2.2: Illustration of crystalline (a), poly crystalline (b) and amorphous (c) MOF thin films.

2.2 Principles of photocatalysis and CO_2 photo-reduction

In general, photo-catalysis can be referred to as the acceleration of a photo-chemical reaction with the presence of a catalyst. Photo-catalysts can use light to create electron-hole pairs (exciton). The electrons that are induced can be used in oxidation reactions where as the holes can adopt electrons and perform reduction reactions. A typical photo-catalytic reaction consists of three events:

- The harvesting of light.
- The formation of an exciton.
- The (redox) reaction of the reactants with the induced charge carriers.

These three subjects should be optimized to create a decent photo-catalyst [17] [18].
Photo-catalysts are typical semi-conductors. A material is a semi-conductor if the valance band of the material is full and the energy difference between the valance band and conduction band (bandgap) is smaller than 3,5 eV (354 nm). The bandgap should not be too low otherwise it will get a more conductor-like character [17].
The bandgap of the material plays an important role for the performance of a photo-catalyst. The bandgap determines what wavelengths (what energy) is required to induce an exciton. A common well-known photo-catalyst is titania, which has a bandgap of 3,2 eV (387 nm) [17]. This means that this material is able to absorb light with a wavelength equal to, or lower than, 387 nm. For catalytic (redox) reactions to occur, the potential of the valance band should be higher than the potential of the oxidation reaction. In this way, it is energetically favorable for the valance band to donate an electron to a (reducing) reactant. Similar to this, the potential of the conduction band should be lower than the potential of the reduction reaction. Because the conduction band lies at lower energies, the electrons of the oxidation agents will be collected by the conduction band.
Reduction of CO_2 is a complex process. The typical chemical reduction pathways require reducing species such as water or hydrogen for the donation of electrons. Reduction of CO_2 can yield different products. In the equations below, various ways of CO_2 reduction pathways are given including the oxidation reactions of hydrogen and water [19]. The values of the energies (E, in electron volts) are reported versus a normal hydrogen electrode (NHE) at pH=7, 25°C, 1 atm and 1M of each participant in the reaction apart from H^+.

$$\begin{aligned}
&CO_2 + 2H_2 + 2e^- \rightarrow CO + H_2O, E = -0,53V \\
&CO_2 + 2H_2 + 2e^- \rightarrow HCO_2H, E = -0,61V \\
&CO_2 + 6H_2 + 6e^- \rightarrow CH_3OH + H_2O, E = -0,38V \\
&CO_2 + 8H_2 + 8e^- \rightarrow CH_4 + 2H_2O, E = -0,24V \\
&H_2 \rightarrow 2H^+ + 2e^-, E = 0,00V \\
&H_2O \rightarrow 2H^+ + 0,5O_2, E = 1,23V
\end{aligned} \tag{2.1}$$

The formation of which products are formed depends on various parameters including reaction conditions and type of catalyst. For the last decades, extensive research on the development of the potential in CO_2 photo- and electro-reduction has been performed [20,21]. Under standard conditions, the Gibbs energy change for the reduction of CO_2 to CO using hydrogen, is only 0.53eV. For photo-reduction this would mean that light with wavelengths of 2339 nm and lower is already enough to break the energy

barrier. A problem however is that CO_2 is not directly reduced to CO but requires the formation of the intermediate CO_2^{*-}. The Gibbs energy for this intermediate requires a potential of 1,90V which is a high energy barrier to overcome [19]. If this barrier is not tackled, the system will start to avoid this boundary by creating side routes. This lowers the reactions potential energy barrier but induces kinetic complexity. We see that some reactions require up to 8 electrons and protons. This increases the number of reaction steps required for the reaction. The life times of the electrons should therefore be relatively long to induce all the side reactions and complete the total reduction pathway. This is one of the major challenges in photo-reduction of CO_2 [20, 22, 23].

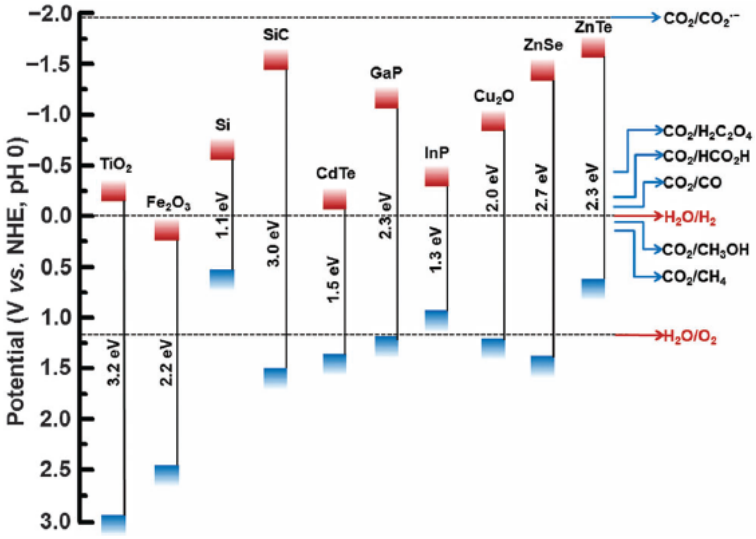

Figure 2.3: An overview of the bandgap positions of different semi conductor materials. CO_2 reduction products are listed at different potential energies. The energies required for the oxidation and reduction reactions of water are included too. Picture reproduced from [20].

In Figure 2.3 the bandgap energies of some common semi-conductor materials is presented [20]. The dashed lines represent the oxidation and reduction potentials of water and some CO_2 reduction products are listed. It can be seen that for the reduction of CO_2 to methanol, TiO_2 and CdTe satisfy the thermodynamic requirements. The potential of the conduction bands of the materials are low and reduction towards methanol is therefore favorable. At the same time, the potential of the valance bands is higher than that of the oxidation of hydrogen (at 0eV). In terms of thermodynamics we can conclude that these two materials are suitable for CO_2 photo reduction towards methanol using hydrogen.

But not only the potential position of the bandgap is important, the width is too. If we consider the solar spectrum, Figure 2.4, we see that wavelengths in the visible region have the highest spectral irradiance (highest intensity). The collection of visible light will therefore be the most convincing method in terms of photo-catalysis of CO_2 or solar fuels in general. A smaller bandgap results in the absorbance of longer wavelengths. The bandgap of TiO_2 (3.2 eV) for example can absorb waves under 387 nm, were the bandgap of CdTe (1.5 eV) can collect waves under 827 nm. A CdTe photo-catalyst looks therefore promising for (near) UV and visible light collection [24]. The expensive and toxic

Cd however, makes this catalyst less attractive. A way to tackle these problems is by constructing a catalyst from two more attractive semi-conductors. An example of this could be a $ZnFe_2O_4/TiO_2$ photo-catalyst [25]. The $ZnFe_2O_4$ has a bandgap of 1.92 eV appearing at band potentials of 0.38 to -1.54 eV. With this, the material can absorb light up to 645 nm. Combined with the high valance band potential of the titania and the low conduction band potential of the $ZnFe_2O_4/TiO_2$, this material is more suitable for redox catalysis compared to the separated materials.

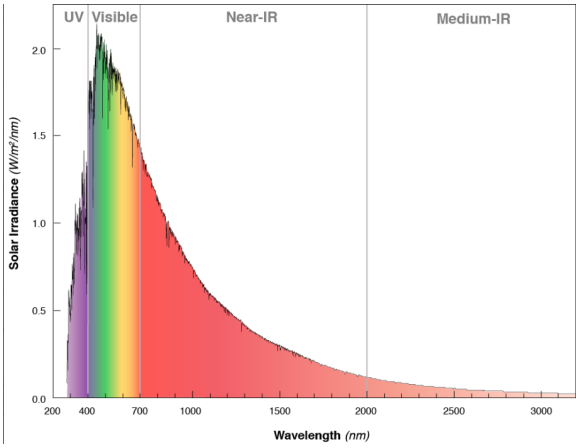

Figure 2.4: Solar radiation spectrum. Light in the visible region is the most abundant at the top of the earth's atmosphere. Picture reproduced from [26].

Besides the thermodynamic conditions and requirements, kinetics play an important role. As mentioned earlier, the formation of an exciton is crucial for photo-catalysis. An exciton is induced when a photon is absorbed by a semi-conductor. An electron in the valance band is elevated to the conduction band leaving a positively charged hole in the valence band. Various events can happen after an exciton is formed. In an unfavorable situation, the charged carriers, holes and electrons, recombine [17]. This can either be done by radiative or nonradiative recombination. With nonradiative recombination the charge carriers diffuse through the material and will eventually find each other and recombine, see Figure 2.5. Radiative recombination occurs when the excited electron relaxes back to the ground state and emits a photon.

For photo-catalysis, recombination is not preferred. A way to prevent recombination is by introducing traps in the material. This increases the lifetime of the excitons and enhances the potential to perform catalysis. A defect in the crystalline material can, for example, be assigned as a trap. This defect acts as an energy well where electrons or holes can get trapped. If the traps are accessible for reactants, the charge carriers can be used in redox reactions.
To shortly conclude this section, the collection of light, exciton formation and choice of catalyst are the main subjects that describe a photo catalysis. Each subject has it own complexity and difficulties and require materials that can combine all the components efficiently and make them work together to create a proper photo catalyst.

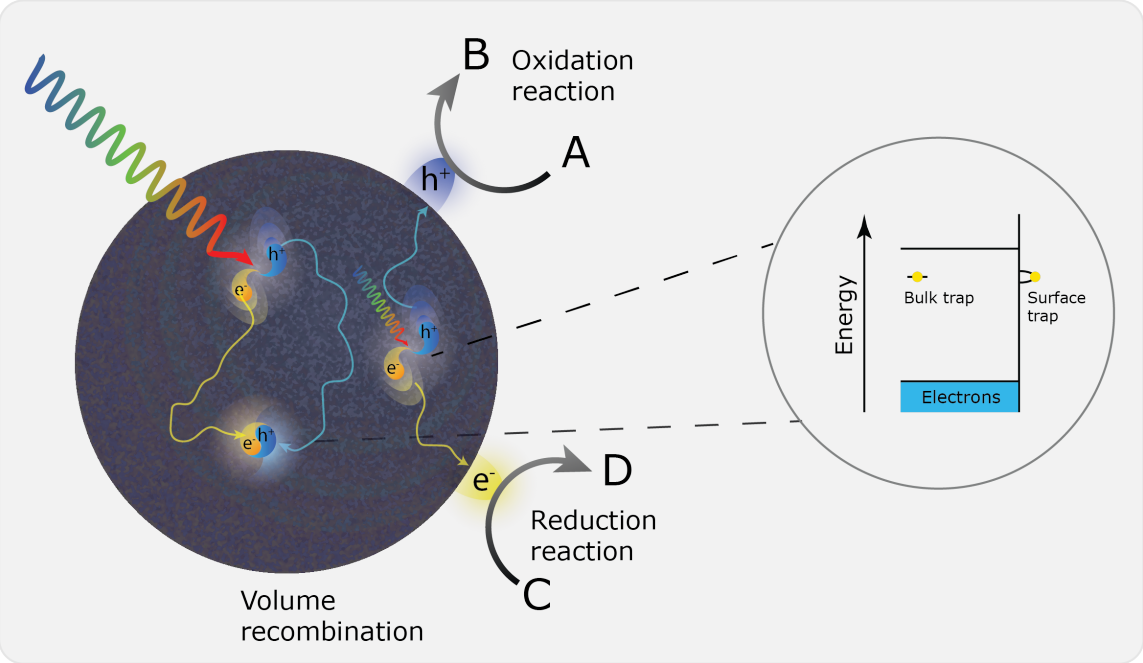

Figure 2.5: A schematic overview of the diffusion of light induced excitons. The charge carriers can move through the material. When the charges meet, the exciton vanishes by volume recombination. If the charge carriers diffuse to the surface, reactions can occur. The electrons can reduce a species, and the holes can withdraw electrons from an oxidation reaction.

2.3 Metal Organic Frameworks for Photo-Catalysis

Metal-Organic Frameworks can not be classified as semi-conductor materials. Semi-conductors are typical photo-catalysts but in most MOFs, there is not always a repeating overlap between orbitals in the crystalline lattice. If this is the case, packing of multiple molecular orbitals creating a valance and conduction band does not occur [27]. MOFs can not be described as organic semiconductors either. In organic semi-conductors, the electronic bands arise due to extended conjugated π bonds. The distance between the organic linkers in MOFs is most often too large and the π orbitals can not overlap.

Conductivity in MOFs

Few studies on the conductivity of MOFs have been performed. These studies show conductivities in the order of 10^{-9}–10^{-3} S cm^{-1}. These numbers roughly fit the conductivity criteria for semi-conductivity (10^{-8}–10^{3} Scm^{-1}) but do not directly make them semi-conductors. Another property of a semi-conductor is the ability to mobilize the charge carriers (excitons). For organic conductors these values start from $10^{-3}cm^2\ V^{-1}s^{-1}$ [28].
A MOF can better be described as crystalline stacking of molecules in a lattice (as recently rationalized by Lin and co-workers [29]). Upon adsorption of light, the excitation can be described as the transition of an electron in the highest occupied molecular orbital (HOMO) to the lowest unoccupied molecular

orbital (LUMO). Considering the two components of a MOF, metal and organic linker, the absorption of light is most often induced by the organic linker. It has been hypothesized that further charge transport could happen via ligand to metal charge transfer (LMCT) [30]. Regarding carboxylic acid coordination, this LMCT is hampered due to the fact that these carboxylic acid groups are isolating (since there is no conjugation character). This is one of the reasons these MOFs show relatively pour charge carrier mobilities. But the charge transport between the linker and the metal can still occur. The electron 'hops' from the linker to the metal node, see Figure 2.6. In this way, MOFs locally transport charges to active sides.

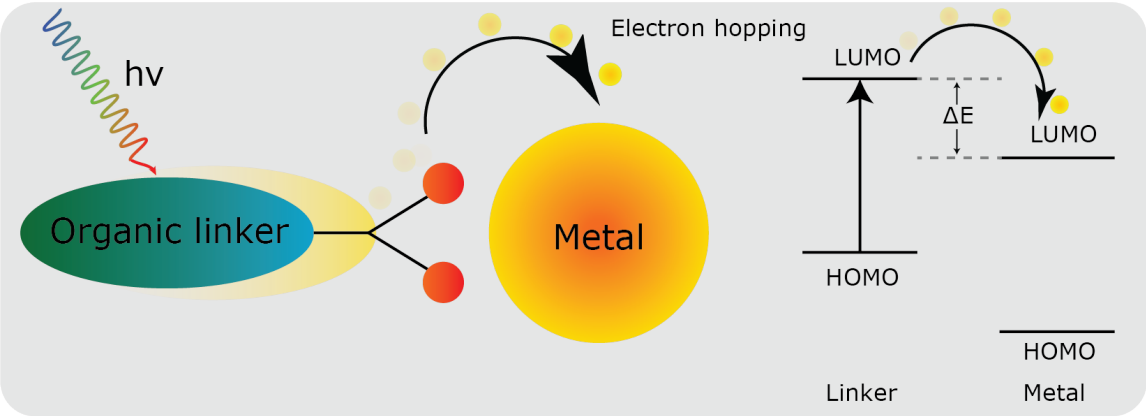

Figure 2.6: The charge transfer in carboxylic acid containing MOFs occurs via electron hopping. The acid group isolate the conductivity between the organic linker and the metal ion.

Optical Tunability

MOFs have a high optical tunability. This means that you can alter the optical properties by changing the organic linkers and metal ions. If the linkers consist of, for example, light harvesting groups such as halides, amine and hydroxide groups the absorption light is stimulated. These substituents have lone pairs that act as an 'antenna'. Organic linkers containing π-bonds can enhance the harvesting of light even more. These π bonds absorb light in the (near) UV region and when these π bonds are constructed in a conjugated manner, the absorption is shifted to visible light. The work of Gascon *et al.* [31] reported these kind of shifts when light harvesting groups and conjugated systems are introduced in a organic linker, Figure 2.7. In the diffuse reflectance UV-vis spectra the influence of such light harvesting groups is clearly visible. MIL-125(Ti) (grey) adsorbs only light below $\pm$300nm, but with the amino-subsequent, NH2-MIL-125(Ti) (orange), the absorption shifts to the visible region. Introducing even more conjugation and lone pairs broadened the absorption area even more, MR-MIL-125(Ti) (red).

Type of Catalysis

To sufficiently use the light and induced electrons, the choice of catalysis is important. Regarding MOFs with light harvesting linkers, three types of catalysis can be considered, as summarized in Figure 2.8. In the first case, the metal or metal cluster is the active component and performs the catalysis. The

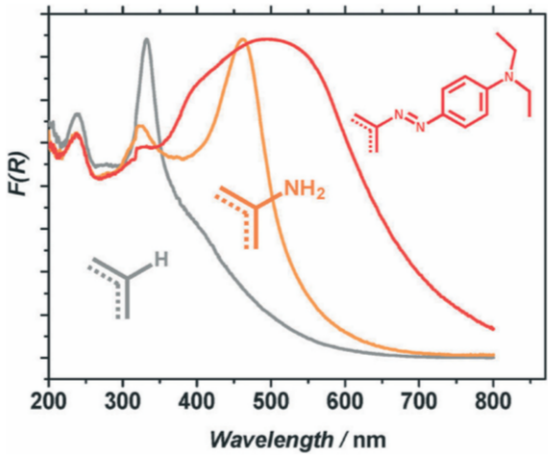

Figure 2.7: Diffuse reflectance UV-vis spectra of MIL-125(Ti) (grey), NH2-MIL-125(Ti) (orange) and MR-MIL-125(Ti) (red). An increase in conjugation within the organic linker leads to a broader absorption area in the visible light region. Image reproduced from [31].

organic linker is used to absorb light and the charges are transported to the metal nodes via LMCT. To create active sites in the metal nodes, defects in the framework should be implemented. The metal nodes are then accessible for sufficient reactant absorption. A way to construct these defects is by using an organic linker with only one coordination unit. If terephthalic acid, for example, is used as organic linker, a fraction of the linker concentration could be replaced with benzoic acid. If the benzoic acid coordinates to a metal (cluster), the construction of the framework at that point will stagnate. The metal will now have a vacant site, suitable for catalysis.
In a second situation, the organic linker both harvests light and performs catalysis. Such properties are observed for porphyrin-based MOFs. These porphyrins are a group of heterocyclic macrocycle organic compounds. Four pyrrole molecules are connected via methine (=CH-) bridges, Figure 2.8b. The position of the nitrogen groups provide a good foundation for coordination to a metal ion. The porphyrins will adsorb the light and donate the induced electron to the metal, whereafter the metal can perform catalysis. The metal can be different than the metal in the framework. This could be an advantage when the active metal is not stable in a framework, for example, but has a (high) activity in catalysis.
The last type of MOF-catalyst with photo-collecting organic linkers is composed of two components: a photo sensitized MOF and a metal or semi-conductor nanoparticle that act as catalyst. The metal particle is encapsulated in the MOF scaffold. The light harvesting groups of the MOF will capture the light and charge transfer provides the electrons to the metal particle and catalysis can occur [30].

Metal Organic Framework Thin Films for Photo-Catalysis

The fabrication of MOFs as thin films, for photo catalysis, has multiple advantages. In many cases, a thin film is preferred over a bulk powder. For example in the construction of a device. Chemical sensors, for example, are built out of electronic circuits and require proper electronic connections. A conductive substrate with a functional coating will provide these terms and create electronic conductivity between

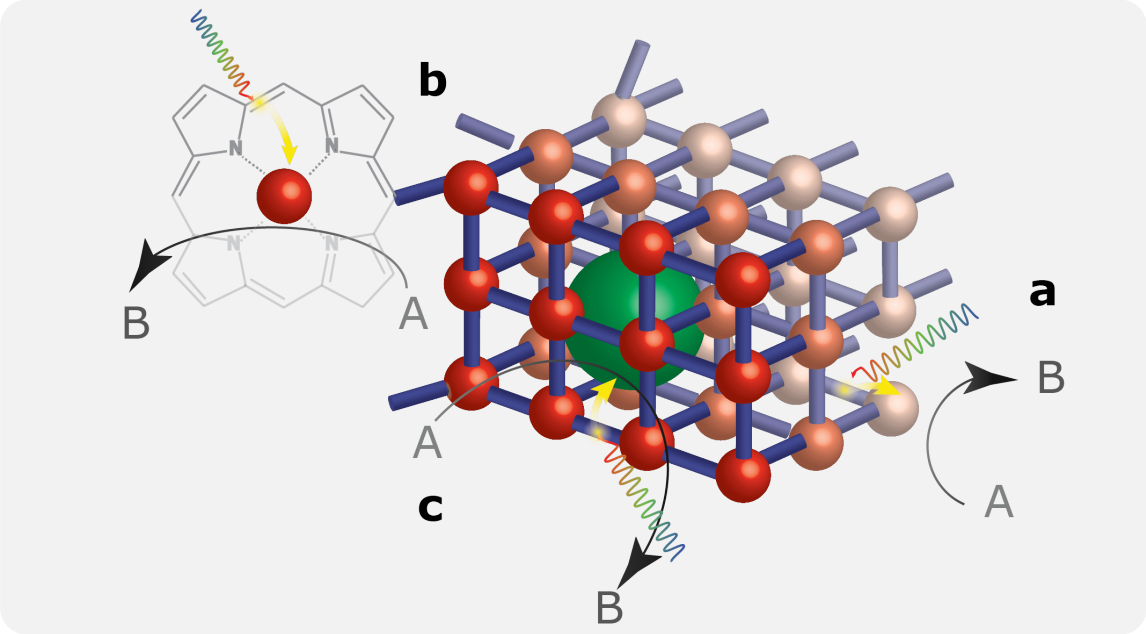

Figure 2.8: Schematic illustration of three types of light driven catalytic reactions on MOFs. a) Light excites an electron at the organic linker and via LMCT the electron is transported to a (vacant) metal side and can be used for reduction reactions. b) The organic linker contains a metal. The linker can both adsorb light and perform catalysis. c) The MOF encapsulates a metal nanoparticle. The MOF harvests light and provides electrons for the metal. The catalysis occurs at the metal particle.

the system and the functional coating. Such constructions are required in photo-catalytic cells as well. The redox chemistry in photo-catalysis relies on a reduction and oxidation reaction. Proper electronic circuits for sufficient electron transport is therefor essential to create a decent photo-catalytic device. [8] Another reason is the accessibility of light to the MOF. In bulk powder, only the surface will be properly emitted by the light. Switching to thin films reduces the amount of material and provides good surface coverage for light collection.

2.4 Preparation of MOF thin films

There are many techniques to synthesize MOF films such as: direct synthesis [32], seeded growth [33], electrochemical methods [34], Liquid-phase epitaxy [35] spin coating (SC) [36], and liquid layer-by-layer (LbL) deposition [37]. LbL and SC were used in this work to prepare the MOF thin films.

Liquid layer-by-layer

Liquid layer-by-layer (LbL) is one of the synthesis approaches to prepare thin film materials. With LbL, coating of only a monolayer can be achieved. LbL synthesis can be described in different stages. First, a (functionalized) substrate is immersed in the solution and the substrate remains in the solution for a certain time. The solute can assemble on the surface of the substrate. When the substrate withdraws

from the solution the solvent drains from the surface and the solute can anchor to the surface of the substrate [38, 39].

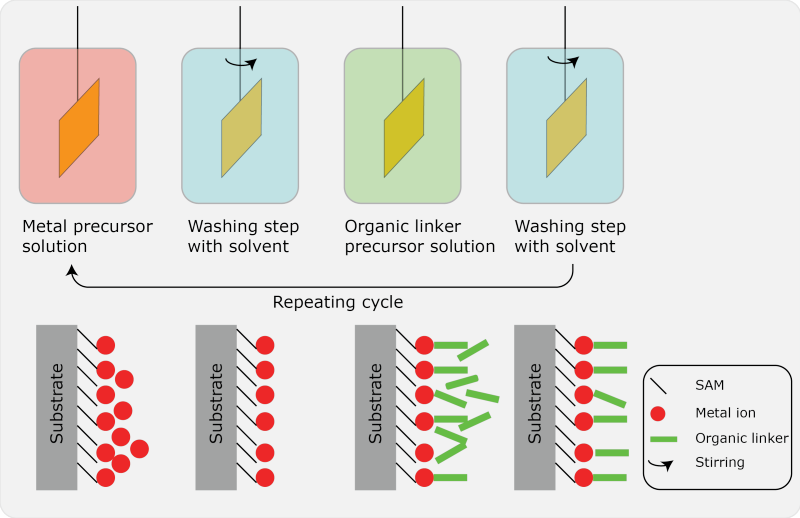

Figure 2.9: Schematic overview of the layer-by-layer synthesis of MOF thin films. Typically, substrates are functionalized with a self assembled monolayer (SAM). The substrates are immersed in the metal precursor solution. Subsequently, the substrates are washed with the solvent. The same processes occur with the linker solution. This cycle is repeated to create a preferred layer thickness.

For the synthesis of MOFs, typically two precursor materials are required: the metal and the linker precursor. The LbL cycle will therefore consist of multiple solutions. First, a substrate will be immersed in the metal solution whereafter it will be dipped in the linker solution. The substrate can be washed in between to remove any excess precursor (and reduces the contamination of both solutions). A typical LbL cycle can be described as follows: dipping in the metal precursor solution, washing with the solvent, dipping in the linker solution, washing in the solvent, see Figure 2.9. When preferred, a drying step can be incorporated in between. This can, for example, be incorporated after the immersing in one of the precursors. Evaporation of the solvent could result in a better attachment of the solid on the surface of the substrate but can also lead to accumulations of the precursors.
There are many variables that can be controlled in layer by layer synthesis such as precursor components and concentrations, solvents and solvent mixtures, amount of cycles, dip time and frequency, washing steps, time and agents. All these parameters result in flexible synthesis routes but simultaneously create complexity.

Spin coating

Another way to prepare thin films is spin coating (SC). In this technique, the coating material is dissolved or dispersed in a solvent. A droplet of this solution is added to a substrate. The spin coater will rotate the substrate and due to the centrifugal force the solution will spread over the substrate and at the same time evaporate the solvent. There are two types of spin coating: static and dynamic. With static SC, the solution is added to the substrate where after the substrate is rotated. For dynamic SC,

the substrate is already rotating when the solution is added [36, 40].

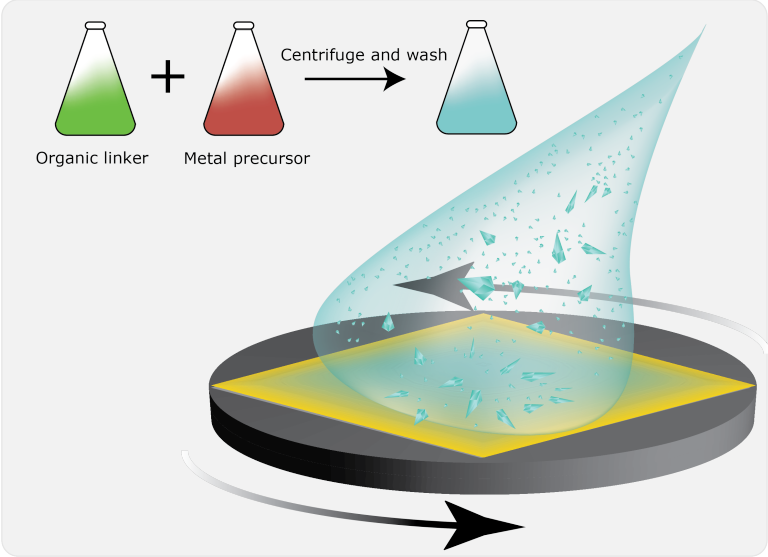

Figure 2.10: The MOF thin film precursors are mixed and after centrifuging and washing steps, the dispersion is spin coated over a gold substrate or FTO glass. The solvent evaporates and the solute remains on the substrate.

Methodology

This section is dived in three parts. First, the synthesis routes and parameters are discussed. Following various characterization methods and techniques that have been used are described. Finally, the methodology on catalytic testing is explained.

3.1 Synthesis

Chemicals

The following chemicals were ordered from Sigma Aldrich:
Cobalt(II) acetate tetrahydrate ($CoAc_2 \cdot 4\,H_2O$) 98.0%, tetrabutylammoniumbromide (TBAB) 98.0%, 2-hydroxyterephthalic acid (MHTA) 97.0%, 2,5-dihydroxyterephthalic acid (DHTA) 98.0%, 4,4 dipyridyl (44BP) 98.0%.

The following chemicals were ordered from Acros Organics:
Cobalt(II) chloride hexahydrate ($CoCl_2 \cdot 6\,H_2O$, 2-aminoterephthalic acid (ATA) 99+%, Methylene Blue certified (MB).

10x10 mm gold substrates were ordered from AMOLF. The substrates consisted out of a (bulk) silica surface (100) with a 2 nm gallium coating and a 60 nm layer of gold.

Fluorine-doped tin oxide glass (FTO, grade TEC 15) was ordered from Pilkington.

Substrate preparation

Gold substrates and fluorine doped thin oxide glass (FTO) were used as substrates to deposit the SURMOFs. The gold substrates were cleaned by consecutively immersing them in acetone, water and ethanol for 30 seconds, after they were treated in UV-ozone for a minimum of 20 minutes. The gold substrates were functionalized with thiol based self assembled monolayers (SAMs) [41]. Acid functionalized gold substrate were prepared with 16-mercaptohexadecanoic acid (MHDA) and 4-mercaptobenzoic acid (MBA). An amine functionalized gold substrate was obtained with 4-mercaptopyridine (MPy). To create a SAM on the gold substrate, the substrates were immersed for two days in 2 mL 0.1 mM MHDA with 1% HAc, 1 mM MBA or 1 mM MPy. Ethanol was used as solvent. The substrates were washed in the solvent and blown dry using 5 bar N_2.

FTO substrates were cleaned by consecutively immersing them in a 1:1:1 v% ethanol:water:acetone solution, 1M HCl solution and water. The solution was sonicated for 10 minutes in every step. The FTO glass was blown dry with 5 bar N_2 and treated with UV-ozone for at least 20 minutes.

Liquid layer-by-layer

MOF thin films synthesized by a liquid layer-by-layer approach were prepared using a HO-TH-03S SILAR coating system with stirrer. For all syntheses, 500mL beakers were used with a dip withdrawal speed and rotational speed of 16mm/s and 60deg/s respectively. During the washing steps, the substrates stirred with a speed of 150rpm.
Cobalt 4,4'-bipyridine (Co44BP) was prepared by first immersing a substrate (functionalized gold or FTO glass) in a 150mL 1mM solution of cobalt chloride hexahydrate in ethanol for 2 minutes. Then, the substrate was washed in ethanol for 10 seconds. After that, the substrate was immersed in a 150mL 1mM 4,4'-bipyridine in ethanol solution for 1 minute. Finally, the substrate was washed again in ethanol for 10 seconds. This cycle was repeated for 50 times.

Spin coating

For the preparation of MOFs using spin coating, the metal and linker precursor solutions were first combined and then three times centrifuged (4000 rpm, 3 minutes) and washed with 30 mL ethanol. After the washing steps, the residues were re-dispersed in 5 mL ethanol. The solutions were spin coated dynamically on the substrates with a 2500 rpm spin speed on a E441 Ossia spin coater. For the gold and FTO substrates, respectively, 20μL and 40μL volume units were used per spin cycle (the FTO substrate had a bigger surface). For further reference: one volume unit is referred as to one layer. The time between every droplet is about 5 seconds. The MOF thin films have typically 20 layers.
Cobalt 2,5-dihydroxyterephthalic acid (CoDHTA) thin films are prepared combining 10 mL, 10 mM DHTA and 10 mL 5mM $CoAc_2$ in ethanol. After at least waiting 15 minutes, the mixture was washed as described above and thin films were obtained.
Cobalt 2-aminoterephthalic acid (CoATA) thin films are prepared combining 10 mL, 10 mM ATA and 10 mL 5 mM $CoAc_2$ in ethanol. After at least waiting 15 minutes, the mixture was washed as described above and thin films were obtained.

3.2 Characterization

Dynamic light scattering

Particle formation and growth of the cobalt MOFs in solution were measured with dynamic light scattering (DLS). The measurements are performed by mixing the cobalt precursor solutions with the organic linker precursors. After mixing, the samples were measured using a cycle program. Every minute a DLS measurement was performed up to 25 measurements. For CoDHTA: 0.05 mL $CoAc_2 \cdot 6\,H_2O$ was added to 1 mL 0.1 mM DHTA just before measuring. For CoATA: 0.05 mL $CoAc_2 \cdot 6\,H_2O$ was added to 1 mL 0.1 mM ATA just before measuring. Room temperature DLS measurements were performed on a Sysmex Malvern Zetasizer with a 10 mW 633 nm laser.

Scanning electron microscopy

For the visualization of the MOF thin films in the nanometer scale, scanning electron microscopy (SEM) was performed. The SEM images were obtained with a FEI Helios nanolab 600 DualBeam mictroscope. The electron beam was operated at 2.00 kV at a current of 0.10 nA. The images were obtained from the secondary electrons with a dwell time of 50, 100 or 200 µs depending on the magnification.

X-ray diffraction

To investigate the formation of crystalline or armorphous MOF thin films, X-ray diffraction measurements were performed. The room temperature XRD measurements were carried out on a Bruker-AXS D2 Phaser powder X-ray diffractometer, in Bragg-Brentano mode, equipped a Lynxeye detector. The radiation used was Cobalt $\kappa_{\alpha 1,2}$ (λ= 1.79026 Å) operated at 30kV and 10 mA using a $\Theta - \Theta$ system with a 141 mm radius and 2.5° sollerslits.

IR-spectroscopy

To investigate the changes in chemical bonds, IR spectroscopy was performed. IR spectroscopy is an important tool for the analysis of MOFs. When an organic linker coordinates to a metal ion, the electronic structure of some bonds of the linker changes. For example, for MOFs with acid based organic linkers, the vibration of the acid groups will change during the formation of a coordination bond with the metal ion. This change can be detected with IR. For MOF thin films deposited on gold substrates, IR reflectance Absorbance Spectroscopy (IRRAS) was used. These coatings often consist of only a few nano meter and are therefore difficult to detect with conventional IR instruments (such as ATR). In IRRAS, the IR beam is guided with mirrors to irradiate a relatively large fraction of the surface of the thin film.
A PelkinElmer Spectrum 1 infrared spectrometer was used to measure the IRRAS spectra. The beam is guided with a grazing angle specular reflectance accessory (Specac) and the beam is detected with a mercury cadmium telluride (MCT) detector. The detector was cooled with liquid nitrogen. Nitrogen gas was flushed in the sample and optics compartments to purge out oxygen and water vapor. The incident IR beam was p-polarized with a grazing incidence angle of 80°. All spectra were recorded with 4 cm^{-1} spectral resolution, 450–4000 cm^{-1} range, with typically 50 accumulations.
For FTO thin films ATR measurements were performed. The measurements were carried out on the same machine but with an ATR accessory.

Raman spectroscopy

To gain more vibrational data, Raman spectroscopy was performed. The symmetric vibrations that are more difficult to observe in IR spectroscopy can be detected with Raman. The measurements were performed on a Renishaw InVia Raman microscope, using 785 nm diode laser excitation through a 50x objective (0.75 NA). The described experiments were all performed under 0.24 mW ($1.12*10^5$ Wcm^{-2}), with 10 seconds integration time.

AFM-IR

To investigate local spatial and chemical differences on the surfaces of the MOF thin films Photo-induced Force Microscopy (PiFM) measurements were performed. The PiFM measurements were operated on a VistaScope from Molecular Vista, Inc. Topography and PiFM images (5 x 5µm2, 256 x 256 pixels) were taken in dynamic non-contact mode using NCHAu tips (Nanosensors) with a scan speed of 0.4 Hz. A Block Engineering tunable quantum cascade laser (QCL) was used as mid-IR source. Detection of topography signal was tuned to the second-, and IR signal detection was tuned to the first mechanical mode of the AFM cantilever. By using independent eigenmodes for detection, simultaneous collection of topography and PiFM signal was realized. The AFM/IR images were analyzed using SurfaceWorks software.

ToF SIMS

Local surface analysis was performed using Time of Flight Secondary Ion Mass Spectrometry (ToF-SIMS). The measurements were performed for chemical mapping of Co44BP in the μm scale. This technique provides MS measurements on thin films. The ToF SIMS measurements were performed using an IONTOF TOF-SIMS 5 instrument equipped with a 30 keV maximum energy bismuth (Bi_3^+) liquid metal ion gun.

UV-vis spectrometry

To monitor the electronic changes during the formation of the MOFs in solution, cuvet UV-vis measurements were performed. The measurements were performed on a Cary 60 UV-vis spectrophotometer from Agilens Technologies. Measurements were performed in the range of 500-200nm or 800-200nm. For cyclic measurements a cycle time of 1 minute was used with an average time of 0.0250 seconds. A data interval of 0,5 nm was chosen with a scan rate of 1200 nm/min. The growth of CoATA was carried out by mixing 0,1mL 5mM $CoAc_2 \cdot 4\,H_2O$ and 2mL 0,1mM ATA in ethanol. For CoDHTA 0,1mL 5mM $CoAc_2 \cdot 4\,H_2O$ was added to 2mL 0,1mM DHTA in ethanol. The growth of Co44BP was prepared by adding 0,2mL 5mM $CoCl_2 \cdot 6\,H_2O$ to 2mL 0,1mM 44BP in ethanol.
The light absorption performances of the MOF thin films were investigated with Diffusive Reflection UV-vis (DRUV). The measurements were preformed on a Lambda 950 S spectrophotometer from Perhin Elmer. Measurements were performed in the range of 800-200nm.

Transient absorption spectroscopy

To get information on exciton half-life times, transient absorption spectroscopy (TAS) was performed. In Appendix 1, a short description regarding this technique is provided.
TAS measurements were performed on an EOS spectrophotometer. A 1064nm laser is used as pomp laser. A harmonic generator splits the laser in separate beams of 266, 355 and 532nm. In the measurements, the 266nm laser is used with a pulse rate of 1kHz with a duration under 1,8 ns. A LEUKOS super continuum light source is used to generate the probe pulse. The spectral acquisition lies between 350 and 850nm with a spectral resolution of 1,5nm. The pulse of the probe laser is set to 2kHz with a duration below 1,2ns. The life times were obtained by fitting a kinetic model to the data points. The model used a polynomial based on the mathematical functions $Ae^x + Be^y + ...$ where x and y are variables that can be extrapolated to half-life times and A and B will give the amount the half-life times contribute to the system.

DFT calculations

To further investigate the type of coordination between cobalt and organic linker, quantum chemical calculations were performed. To reduce the computational demand, the organic linker structures were limited and contain only one acid group and one substituent. For DHTA this means that 1-hydroxy benzoic acid is used and for ATA, 1-aminobenzoic acid. For all cobalt complexes an octahedral coordination geometry is assumed while the electron configuration is Co(II) low-spin. All quantum chemical simulations were spin-unrestricted and were performed using DFT with the global hybrid functional B3LYP [42, 43] and a non-augmented triple ζ basis set [44, 45] implemented in the ADF program. No electron approximations were made (no frozen core) and the numerical quality was 'good'.

3.3 Catalytic testing

CO_2 photoreduction with GC gas detection

The photo catalytic performance of CoDHTA@FTO for the reduction of CO_2 was tested in a photo catalytic setup. An artificial sun was used to illuminate the MOF thin film. A solar simulator Oriel Sol3A 450W with 101 x 101 mm beam size calibrated to 1 sun (100 mW/$cm2$) was used. A gas mixture of 0,5mL/min CO_2 and 2mL/min H_2 was used as reactant. (H_2 was chosen in stead of water, because the MOFs were not stable in aqueous solutions.) The output gas of the reactor was filtered by an aerosol filter before injecting it in an InterScience Compact Gas Chromatograph (GC). Every 4 min, a sample of the output gas was injected in the GC and analyzed by FID detectors. Two column systems were used to measure either hydrocarbons on one end and $CO/CO_2/CH_4$ on the other. The latter was equipped with a methanizer to visualize each component.

Electro-reduction of methylene blue

The electro-catalytic performance of CoDHTA@FTO was investigated using dye degradation with methylene blue (MB) [46]. In this reaction, see Figure 3.11, the -N=C- group of the thiazine is reduced to a -NH-CH- group. This requires two hydrogen atoms and two electrons.

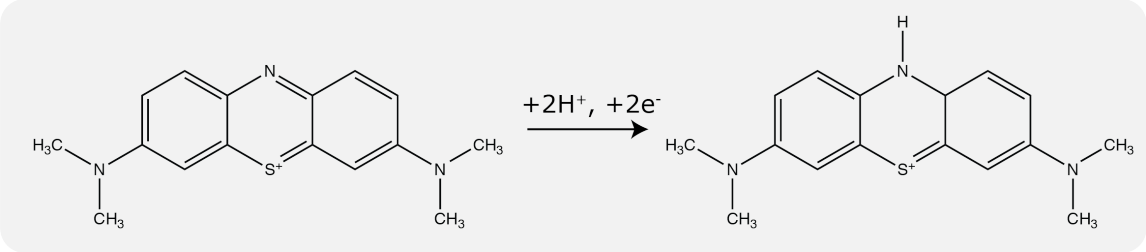

Figure 3.11: Schematic illustration of methylene blue reduction.

For this reaction, a 100 mL solution of 5,7 mgL^{-1} MB was prepared. MB act as dye and reducing reactant. Then, 807 mg tetrabutylammonium bromide (TBAB) (±0m1M) was added as electrolyte. Ethanol is used as solvent. Just before the reaction, 1 mL 30% hydrogen peroxide (an excess) was added as oxidation agent.
Electro-catalytic measurements were performed using a two electrode setup consisting of a working electrode (WE) and a counter electrode (CE). The setup is illustrated in Figure 3.12. The reactor was filled with ±100 mL of the reaction mixture. The FTO glass coated with CoDHTA was cut into 1x1.5 cm pieces. A special holder was used to hold the FTO glass piece in the solution and electronically connect it to the reaction setup. For clarity, CoDHTA@FTO acted as working electrode. The position of the CoDHTA@FTO was immersed relatively in the upper layer of the solution. A pure platinum grid was used as counter electrode. The grid was cleaned before use with a gas burner. Before the experiment, the reaction container was flushed with argon to purge out oxygen. The reaction time was set to 270 minutes. Transient potentiometry (TP) was used as reaction program. In this program, a constant current was applied between the electrodes and the induced potential during the reaction was measured over time. The current was set at 100 μA. The principles of TP relay on redox reaction at the electrodes. The electrons provided by the cathode do not simply 'diffuse' trough the solution.

Species located at the anode take up the electrons. At the same time, solutes around the cathode provide electrons to create a electric cycle. For the reduction of MB, this means that MB withdraws electrons at the anode (reduction) and H_2O_2 provides electrons to the cathode (oxidation).
During the reaction, cuvet UV-vis samples were taken to analyze the concentration MB. The volume of these samples were around 2 mL. The concentration MB could simply be followed because the absorbance is directly proportional to the concentration according to Lambert Beer's law:

$$A = Cd\epsilon \tag{3.2}$$

where, A is the absorbance, C the concentration, d the path length of the light and ϵ the absorption-coefficient.

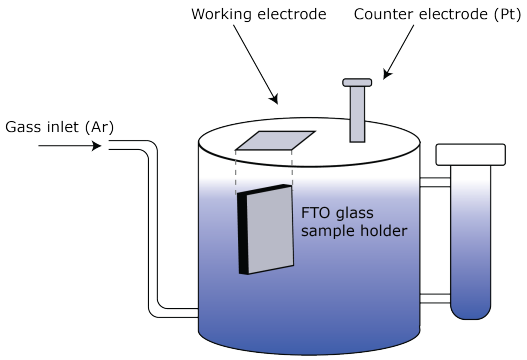

Figure 3.12: A simplified schematic illustration of the electro-catalytic setup. In this setup, two electrodes were used. CoDHTA@FTO acts as the working electrode and a Pt-electrode performed as counter electrode. Before the catalysis, the reactor is flushed with argon to purge out oxygen.

The reaction time of MB reduction under the catalytic presents of CoDHTA@FTO can be theoretically calculated. In this calculation, we assume that all electrons, that are generated in the transient potentiometry setup, are used for the reduction of MB. Equation 3.3 is used to calculate the time.

$$Reationtime(seconds) = \frac{M[moldm^{-3}] * V[dm^3] * F[Cmol^{-1}]}{I[Cs^{-1}]} * n_{elec} \tag{3.3}$$

In this equation, M is the concentration MB in the solution, I the applied current, V the volume of the solution, n_{elec} the amount of electrons required per MB molecule and F the Faraday constant, 96485.3329 coulombs per mole.
The concentration MB was 5.7 mgL^{-1}, which equals 17.8*$10^{-6}molL^{-1}$, the volume was 100 mL and the current was set to 100 $*10^{-6}$A. Figure 3.11 demonstrates that two electrons are required for the reduction. If these values are applied to equation 3.3, a reaction time of 57.24 minutes is obtained. Thus, this means that if all electrons are used for the catalysis, MB should be completely reduced in 1 hour.
To investigate the influence of the FTO glass during the reaction, the same process is repeated using only bare FTO glass. Subsequently to this, the same reaction was performed without electro-catalysis. This experiment was done by simply adding the chemicals together and measure the absorbance of MB over time.

Structural Results

The appearance of the MOF thin films was captured with scanning electron microscopy (SEM), figure 4.13. For Co44BP and CoDHTA, relatively small rod-like / rectangular crystals were observed. The surface of CoDHTA seems to consist of two types of solids: the needle-like crystals and a more bulky accumulation of these crystals. This was not observed for Co44BP. This accumulation of crystals could be the consequence of spin coating. Small crystals in the droplet are whirled over the substrate surface and will anchor to the surface groups. But if the surface already contains these crystals, the crystals in the droplet "stick" to the crystals on the surface and cluster. In the case of Co44BP, a surface covered with closely stacked small crystals was observed, as seen in figure 4.13a. The LbL-synthesis provides more growth time, and the crystals can grow via a bottom-up approach: nucleation on the surface followed by a controlled growth. This resulted in a more ordered Co44BP surface compared to CoDHTA. For CoATA, we do not see any kind of structure. In Appendix 3 and 4 more SEM images of Co44BP and CoDHTA are presented showing more scaling lengths.
We can classify the images in three types of MOF thin films. The first SEM image, 4.13a, can be referred as SURMOF: we observe a compact relatively homogeneous film of crystals. The middle image, 4.13b, is a polydispersed MOF thin film. The surface is covered with various sizes of crystal-like MOF structures. The last picture shows no specific structure, 4.13c. A powdered sugar-like structure covers the surface. In the coming sections, these observations are explained for each MOF thin film.

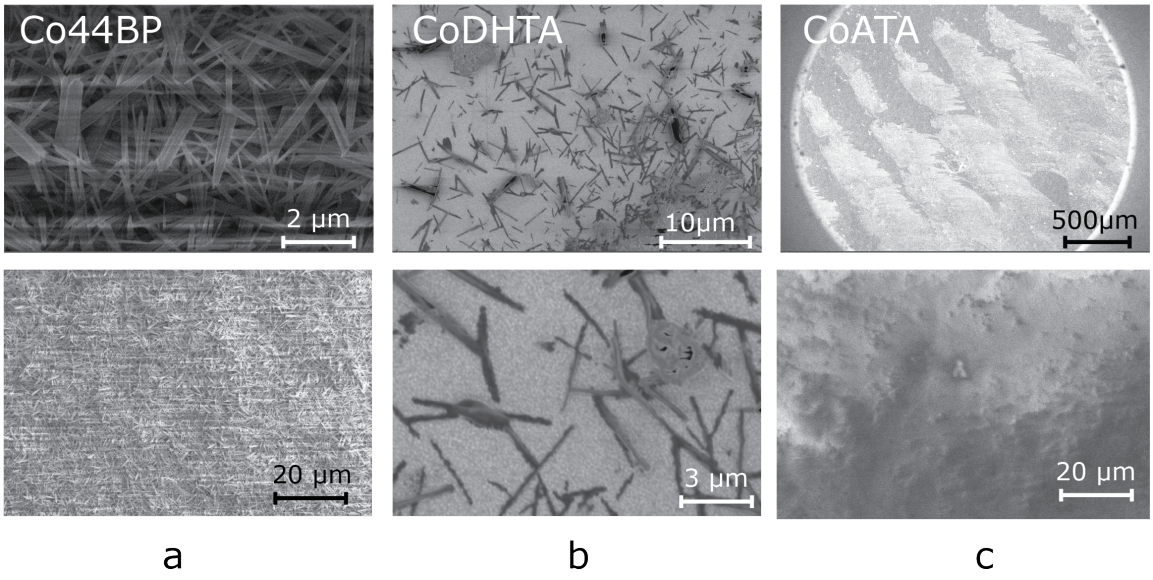

Figure 4.13: SEM images of a) Co44BP@MHDA. A homogeneous coating was observed b) CoDHTA@FTO. This surface appeared more like a poly crystalline MOF. Various sizes and randomly distributed crystals were spread over the surface. c) CoATA@FTO. No clear structure was observed. The coating looks like powdered sugar.

4.1 Cobalt 4,4'-bipyridine

The synthesis of Co44BP was prepared with a liquid layer-by-layer synthesis approach. The Co44BP SURMOFs were grown on three different substrates. Gold substrates functionalized with *p*-mercapto-benzoic acid (MBA) and *p*-mercapto pyridine (Mpy) were used as model systems to create an acid and amine functionalized surface respectively. FTO glass, terminated with -OH groups was used too, because this substrate is relatively strong and is more suitable under catalytic conditions compared to the gold substrates. After the synthesis IRRAS measurements were performed to investigate if the 44BP coordinates to the cobalt.

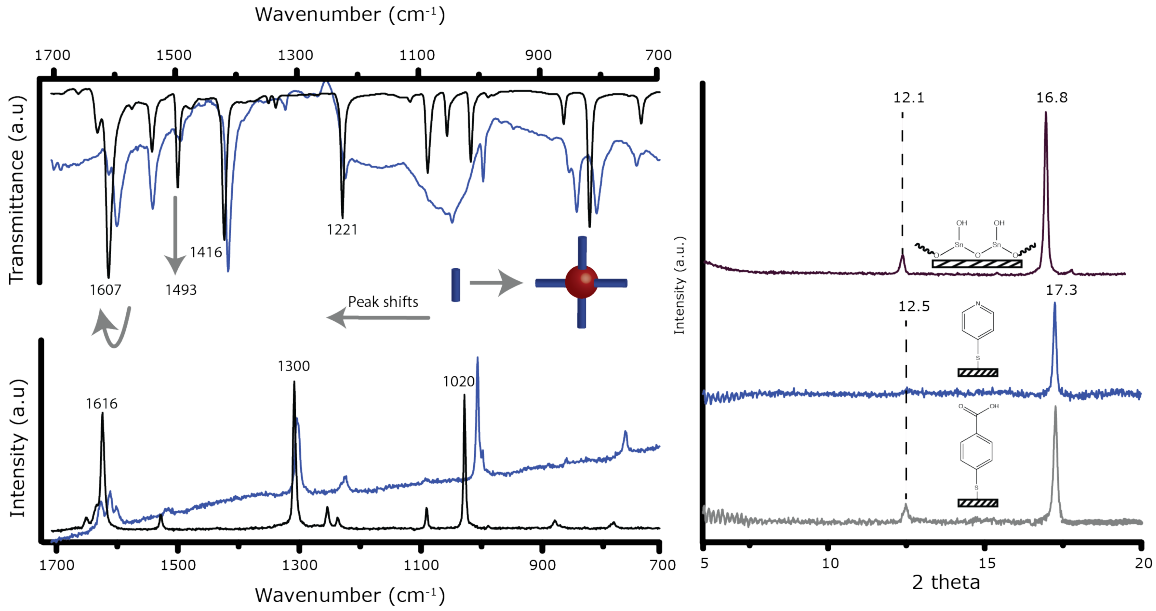

Figure 4.14: Left: IR (top) and Raman (bottom) spectra of 44BP (blue) and Co44BP (black). Right: XRD diffractograms of Co44BP on MBA, MPy, and FTO glass surfaces.

In the left image in Figure 4.14, the spectra are shown. The blue lines represent the IR and Raman absorption spectrum of pure 44BP between 1700-700cm^{-1}. In the IR spectrum, sharp bands are observed between ±1600-1400cm^{-1} and can be assigned to the ring stretching vibrations (including C=C, C=N stretching vibrations). The broad bands between ±1250-1000 arise due to C-H deformation vibrations and lower energetic C=C and C=N stretching vibrations. Three sharp bands are observed in the Raman spectrum at 1616, 1300 and 1020cm^{-1} and can be assigned to a ring vibrations and two C-H deformation vibrations respectively.
With the introduction of cobalt (II), the spectrum changes as can be observed in the black lines. There are two main observations in the spectra that indicate the formation of Co44BP. First of all, comparing the spectra of 44BP before and after cobalt is introduced, an average blue shift is observed for the IR and Raman spectra. The ring vibration of 1593 to 1609 cm^{-1} in the IR spectra is the most intense

shift. The increase in energy of the vibration indicates an increase in energy of the ring vibration. This increase of the vibrational constant can have several causes. On the one hand, the cobalt ions could donate electrons to the bipyridine, thereby increasing the energy of the ring vibration (back donation). On the other hand, steric hindrance effects can cause the peak shift as well. The direction of the vibration could be hindered due to confinement in the framework. Secondly, the peak at $1488cm^{-1}$ is increasing. This vibration can be assigned to an aromatic C=C stretching vibration. It is not completely clear why this band is increasing but it could be that this typical vibration is more free to vibrate when 44BP is present in a MOF than when 44BP is constructed in a molecular crystal. In the Raman measurements, the bands are blue shifted as well. In agreement with the previous arguments, this average blue shift could be due to the confinement of the 44BP in a framework. The vibrational changes of the 44BP strongly indicates that the 44BP is coordinated to the cobalt(II).
After this confirmation the formation of a crystalline material (a framework) was investigated with XRD measurements on the different substrates. It is interesting to see that the crystallinity of Co44BP is similar on the oxygen containing surfaces of FTO and MBA and on the nitrogen functionalized Mpy substrates, right image Figure 4.14. The direction of the growth of Co44BP crystals appears to be independent of the surface groups. A peak at 17.3° and a less intense peak at 12.5° were observed. Furthermore, the sharp peaks indicate the presence of identical crystalline domains in the SURMOF, indicating a homogeneous growth. To investigate how homogeneous the MOF is distributed over the surface, ToF SIMS analysis was performed.
Chemical mapping using Time of Flight Secondary Ion Mass Spectroscopy (ToF SIMS) reveals a correlating between cobalt(II) and 44BP over the surface, figure 4.15. The Co^+ species are homogeneously distributed over the surface and the $C_{11}H_{11}N^+$ (bipyridine) fractions appear at the same locations as the cobalt fractions. Line scan analysis is performed for visual enhancement. We see over the distance, the intensities of both species correlates quite significant. This indicates even more that the surface is mainly covered by closely stacked Co44BP crystals.

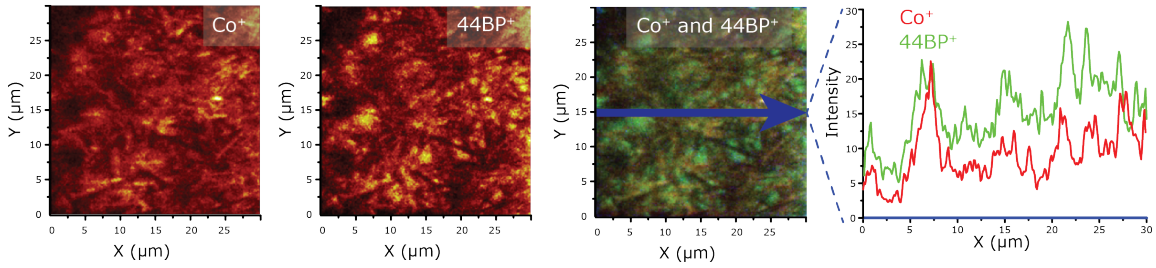

Figure 4.15: ToF SIMS images of Co44BP. The Co^+ and 44BP+ fractions correlate over the whole surface.

With the above described analysis, it can be concluded that Co44BP SURMOFs can be prepared with LbL synthesis at room temperature. The obtained films were homogeneous and cobalt and 4,4'-bipyridine correlate over the surface. The growth of the SURMOF appears to be independent of surface groups, at least the one described above.

4.2 Cobalt DHTA

With spin coating (SC), a polydispersed CoDHTA thin film was prepared, as observed in the SEM image 4.13b. CoDHTA was grown on two types of surfaces: a gold substrate functionalized with 16-mercaptohexadecanoic acid (MHDA) as model system and FTO glass as potential substrate for catalysis. After the synthesis, the substrates were first studied with IR and Raman to confirm the formation of the coordination of DHTA to cobalt(II).

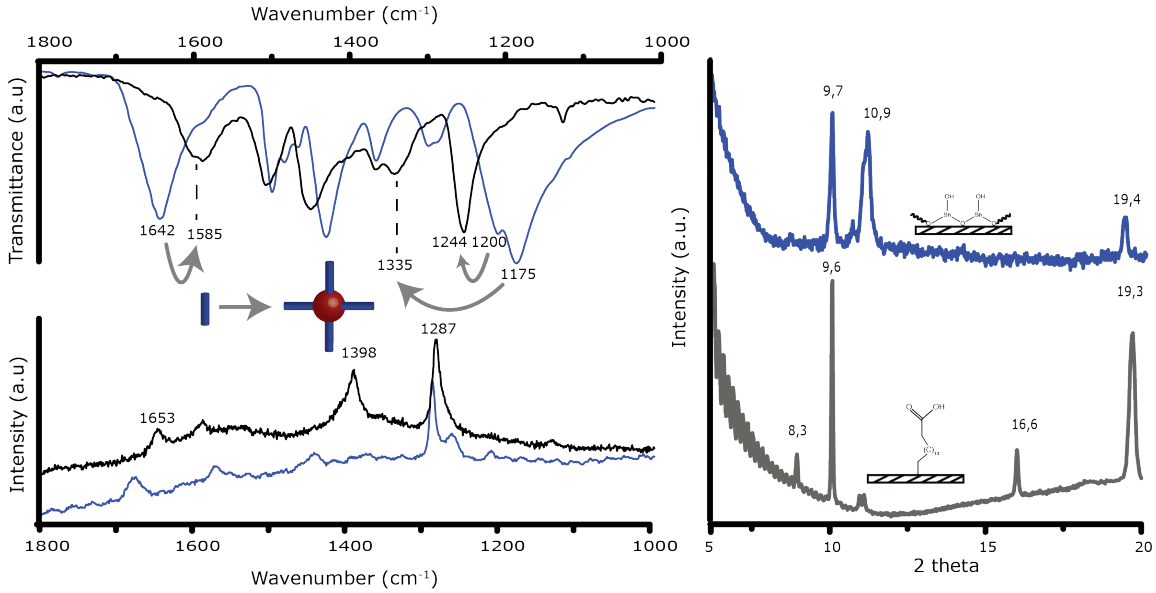

Figure 4.16: Left: IR (top) and Raman (bottom) spectra of DHTA (blue) and CoDHTA (black). Right: XRD spectra of CoDHTA at MHDA (bottom) and FTO glass (top) surfaces.

In the left image of Figure 4.16, the IR absorption spectra of DHTA and CoDHTA are displayed in the region between 1000-1800 cm^{-1}. All important vibrations are listed in Table 4.1. The blue line corresponds to pure DHTA characterized by the carboxylic acid bands at 1642 cm^{-1} (C=O stretch) and 1175 cm^{-1} (C-O stretch). The C-O stretching vibration of the phenol group is observed at 1200 cm^{-1}. The ring vibrations of the benzene are observed in the region between 1300-1500 cm^{-1}. The Ring vibrations (mainly C=C stretching) are observed in three bands in the region ±1500-1450 cm^{-1} and a broad band at ±1420 cm^{-1}. The C-H in plane deformation vibrations rise at 1280 cm^{-1}.
With the introduction of cobalt(II), the spectrum changes. The C=O and C-O stretching vibrations disappear combined with a blue shift of the benzene vibrations. Three new bands have formed at 1585, 1335 and 1244 cm^{-1}. As described for Co44BP, the blue shift of the benzene vibrations could be the result of back donation of cobalt(II) to the ring or due to confinement in a framework. In both cases, this shift is a good indication of the coordination of DHTA to cobalt(II). The band at 1585 cm^{-1} is most likely the COO^- asymmetric stretching vibration of the acid groups coordinated to the cobalt(II). It is interesting to see that both C-O vibrations of DHTA have disappeared. This strongly

Table 4.1: IR vibrations observed for DHTA and CoDHTA. The bands are assigned using the tables in [47].

Vibration band energies DHTA (cm^{-1})	**Vibration bond DHTA**	**Vibration band energies CoDTA** (cm^{-1})	**Vibration bond CoDHTA**
1642	C=O stretch	1585	COO^- assym.
1495	Ring	1505	Ring
1416	Ring	1446	Ring
1201	C-O stretch (Phenol)	1333	COO^- sym.
1175	C-O stretch (acid)	1244	CO^-

indicates that both OH groups of DHTA were involved in the coordination to cobalt (II).
To get more insight in the coordination of DHTA to cobalt(II), DFT calculations were performed. In bottom graphs in Figure 4.17, the calculated IR spectrum for CoDHTA where DHTA coordinates only with the acid to the cobalt (II) is shown. The blue line corresponds to the calculated IR spectrum of DHTA and the brown line is the measured spectrum. We can see that these spectra do not completely match, and many bands appear to be shifted. This is mainly the case because the calculations were performed under vacuum conditions (no external interactions were taken into account). The C-O vibrations in the calculated spectrum are, for example, located at 1086 cm^{-1} (for the acid) and 1293 cm^{-1} (for the phenol). In the measured IR spectrum, these bands appear at 1175 cm^{-1} (acid) and 1200 cm^{-1} (phenol). For this analysis we therefore mainly focused on relative changes. When cobalt was introduced, the calculated spectrum changes. The asymmetric and symmetric COO^- vibrations appear at 1640 cm^{-1} and 1370/1410 cm^{-1} respectively. The shift between the C=O stretching to the COO^- asym. is $\pm 60 cm^{-1}$. This matches the difference for the measured DHTA and CoDHTA. The difference between the C-O stretching to the COO^- sym. stretch is however around 300 cm^{-1}. This is quite high, but is most probably due to calculations without hydrogen bonds taken into account. The calculation, however, indicated that the COO^- symmetric stretching vibration lies significantly higher in energy compared to the C-O stretching vibration. For the measured CoDHTA, this suggests that the band at 1335 cm^{-1} is the COO^- stretching vibration of the acid coordinating to cobalt. This was also confirmed with Raman measurements, Figure 4.16. In the Raman spectra of DHTA, the C=C stretching vibration at ± 1290 cm^{-1} was observed. Some small bands between 1500-1700 cm^{-1} are present and are probably the C=O stretching vibrations. After introduction of cobalt, a band at 1398 cm^{-1} arises which is most likely a symmetric COO^- vibration [48, 49]. The remaining band at 1244 cm^{-1} in the measured IR spectrum of CoDHTA can most probably be assigned to the coordination of the hydroxide of the benzene to the cobalt. Unfortunately, the computational demand was high for the DFT calculations on the coordination of DHTA involving the hydroxide groups. The calculations took a long time and could not be incorporated in this work. Thought out this thesis, however, more evidence in favor of this theory is described.
Subsequently, the crystallinity of the CoDHTA thin films on the different substrates was investigated. In the XRD diffractograms, the 2θ signals of the CoDHTA on MHDA and FTO match at the same diffraction angles. We see signals at 9.7°, 10.9° and 19,4° for both surfaces, right image Figure 4.16. The sharp peaks indicate a the formation of identical crystalline domains. There are, however, a few differences. The ratio between peaks 9.7° and 10.8° is different for FTO and MHDA surfaces. The peak at 10.9° is more intense for Co44BP@FTO. Moreover, we do not observe a peak at 16.6° for Co44BP@FTO. These observations indicate that there is a different preferred direction for CoDHTA crystals on FTO compared to MHDA.

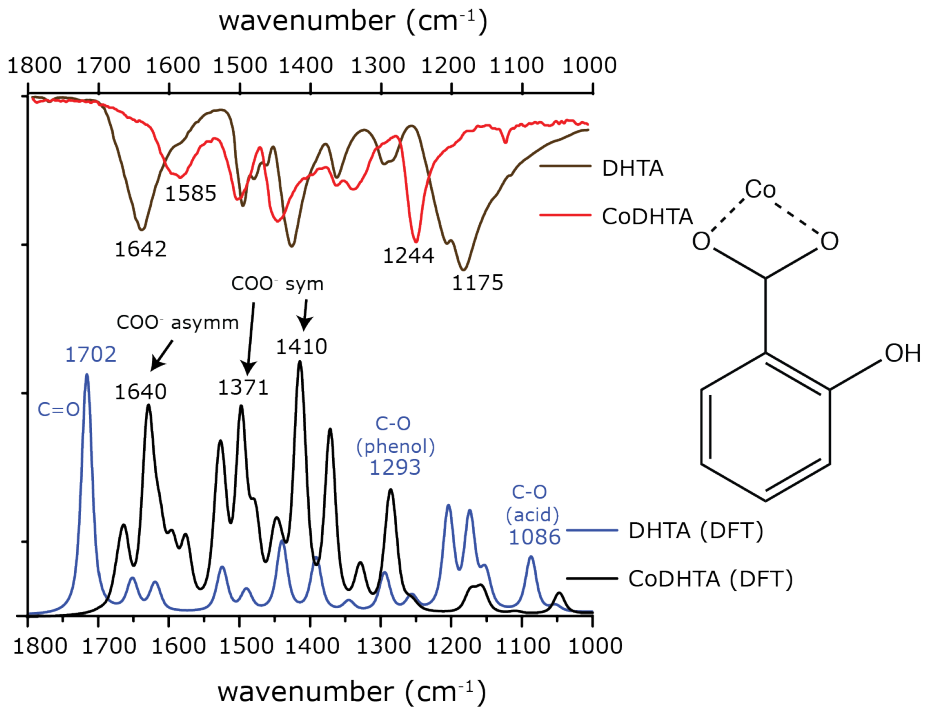

Figure 4.17: Bottom graphs: DFT calculated IR spectra of DHTA (blue) and CoDHTA (black). In the top, the measured IR spectra of DHTA (brown) and CoDHTA (red) were shown.

The structure of DHTA consists of two hydroxide groups and two acid groups all bound to a benzene. The common place to coordinate is to the acid groups but coordination of cobalt could also occur to the hydroxide groups. If both the hydroxide and acid groups are involved in the coordination, it would not be surprising that the direction of CoDHTA crystals at FTO differs from MHDA. MHDA create a surface terminated with acid groups, where FTO has -OH surface groups. During SC, the dispersed crystals will start to anchor to the surface groups. For MHDA, this could mean that the direction of the crystals could be in plane with the coordination of the cobalt with the acid. Vice versa, for FTO, the crystals could anchor in plane with the -OH coordination of the cobalt to the -OH surface groups, see Figure 4.18. To analyze this hypothesis, AFM-IR measurements were performed. With AFM-IR, more detailed information of the chemistry at the surfaces of the CoDHTA thin films could be obtained.
In Figure 4.19 a 5x5 μm AFM image of CoDHTA@FTO is displayed. Most of the image represents mainly the surface of the FTO glass but some high features were observed. At three spots, a PiFM spectrum was collected to investigate the different features. These spectra are shown next to the image combined with the ATR spectra of the CoDHTA@FTO thin film (black line) and DHTA (blue line).

The red and brown lines correspond to the IR spectra of the high features. The peak at 1260 cm^{-1} is an tip-artifact of the AFM-IR (the tip is conserved in silicon oil) and should not be considered as

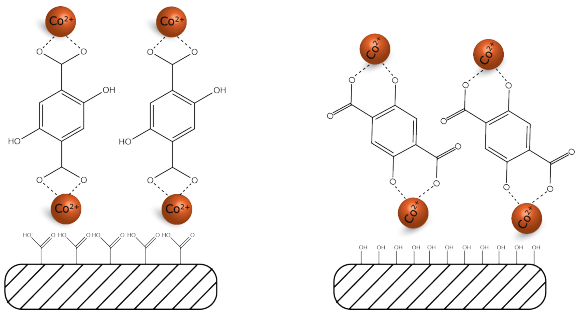

Figure 4.18: Schematic illustration of different coordination possibilities of CoDHTA at acid or hydroxide terminated substrates.

a valid data point. The PiFM spectra match the ATR spectra quite well. The characteristic bands at 1585, 1446 and 1340 cm^{-1} were observed. This suggest that the high features are CoDHTA MOF rectangular-like crystals. The green line represents the IR spectra on the surface of the FTO glass. Some interesting spectral features were observed. There is no band observed at 1585cm^{-1}, only two bands at 1464 and 1340 cm^{-1}. This suggests that the carbonyl is not involved in the coordination. The band at 1340 cm^{-1} (COO^- sym.) is, however, still observed and indicates the presence of coordinated acid to cobalt(II), in a way where only the -OH group of the acid coordinates. Subsequently, the appearance of the ring vibration at 1464cm^{-1} is an interesting phenomenon. This band differs compared to the spectra of the high features where a similar band arises at 1446 cm^{-1}. These bands could both be induced by the same vibration, but are somehow shifted. This shift could be explained by the type of coordination. The electronic structure of the benzene group is influenced by the acid and hydroxide groups. If cobalt(II) coordinates to the acid group, electrons are withdrawn from the acid to form the coordination bond. The electrons in the benzene will compensate this charge difference by donating some charge density to the acid groups. This change in electronic structure has an impact on the vibrational energy of the benzene ring, just as we observe now. The changes in electronic structure of the benzene depends on the way DHTA coordinates to the cobalt(II). For example, if DHTA coordinates only with the acid group, the benzene ring will only donate electrons to the acid groups. But, if DHTA coordinates with both the -OH group and the acid groups, the benzene has to donate charge density to both the acid and hydroxide groups. For both situations, the electronic structure of the benzene changes and for both situations the energy of the ring vibrations is different. We could argue that the vibrational energy of the benzene ring correlates to a certain kind of coordination. Regarding the spectra in Figure 4.19, we could say that when no band at 1585 cm^{-1} is observed, the C=O group of the acid is not involved in the coordination and the ring vibration of the acid appears at higher energies 1464 cm^{-1} than when the C=O groups are involved in the coordination, The ring vibrations are than observed around 1446 cm^{-1}.

Similar results were observed for CoDHTA@MHDA. In the top left image in Figure 4.20, the AFM image of CoDHTA@Au is presented. In the yellow parts, shapes of rectangular-like crystals can be seen, similar to the SEM image 4.13b. At four spots, a PiFM spectrum was taken. The same phenomenon for CoDHTA@FTO was observed here. The ring vibrations were blue shifted when less COO^- asymmetric stretching vibrations were present. In all spectra, the COO^- symmetric stretching vibrations are visible at 1340 cm^{-1}.

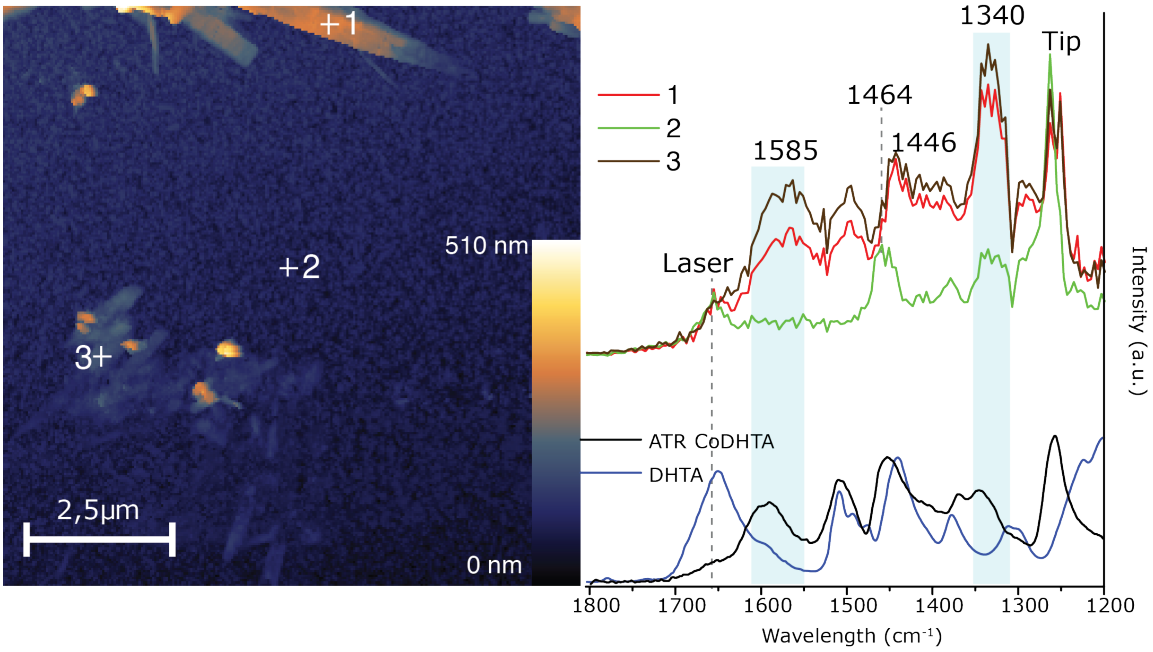

Figure 4.19: AFM-IR image and spectra of CoDHTA@FTO. The IR spectra of the higher features correspond to the ATR measurements. At the surface of the FTO glass, a thin layer of MOF seems to be present. The band at $1585cm-1$ is not present and indicates the presence of uncoordinated carbonyl groups.

We have mapped the type of coordination using the ring vibrations at 1446 cm^{-1}: the higher the signal, the more the ring vibration at 1446 cm^{-1} is present and the more the C=O group is involved in the coordination to cobalt (II). In the bottom image of Figure 4.20, the chemical mapping at 1446 cm^{-1} is shown. The more yellow the color, the more intense the IR signal. We see that this vibration is quite heterogeneous distributed over the surface. At the highest spots, this vibration is not really abundant but appears more at the thinner layers. If we look more closely to the AFM image, we see that at the higher features, the crystals are quite randomly accumulated while in the lower layers, the crystals are more ordered. So, if there is more signal at 1446 cm^{-1}, there are more DHTA molecules that coordinate involving the C=O group. This suggests that more homogeneous distributed CoDHTA coatings were obtained when the C=O group is involved in the coordination. This is, however, not proven yet. More PiFM analysis on the materials should be performed to see if this phenomenon repeats at different spots or different samples.
After analyzing the two surfaces MHDA and FTO separately, some preliminary results on the spatial and chemical differences of CoDHTA on the different substrates could be obtained. The IR spectrum of the green line is taken on a very thin spot and it can be seen that a fraction of a coordinated carbonyl is still present: the band at 1585 cm^{-1} is still visible. This is something what is not visible in the IR spectrum at a very thin layer of CoDHTA on FTO, green line Figure 4.19. It is difficult to argue, but it appears that for this -OOH surface, CoDHTA coordinates involving both the carbonyl and hydroxide of the acid in-plane with the acid groups of the SAM (mercapto-dodecanoic acid). This could be the opposite for CoDHTA@FTO. The coordination could be in-plane with the -OH groups of

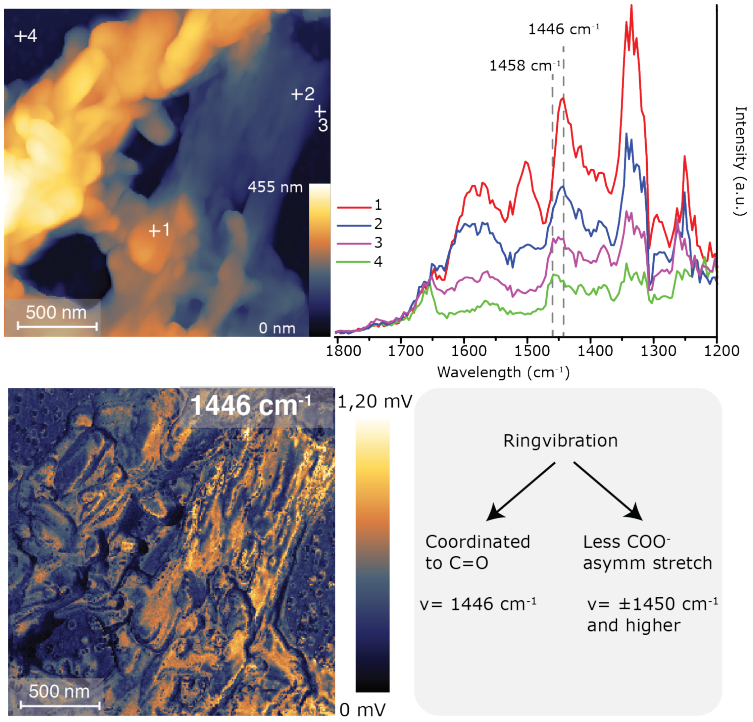

Figure 4.20: AFM-IR images and spectra of CoDHTA@Au. Top left: AFM tomography image. Top right: IR spectra of different spots on the surface. The measurements show that CoDHTA is not homogeneously distributed over the surface. At the higher features, the CoDHTA crystals appear to be accumulated, while on the thinner layers, a more orderly CoDHTA structure had formed. Bottom left: chemical mapping at $1446cm^{-1}$. This ring vibration gives an indication of the type of coordination. The higher the ring vibration, the less the C=O is involved in the coordination. The chemical map shows low energetic ring vibrations at the thinner and more ordered CoDHTA layers. This indicates that more ordered CoDHTA crystals were formed when C=O was involved in the coordination.

.

the FTO glass. This would explain the XRD diffraction patterns observed in figure 4.16. To further investigate this, very thin films on both substrates should be prepared (perhaps only one layer) and with XRD measurements the differences in growth direction should be investigated. Combined with the vibrational data, this would give an good indication about the correlation between the surface groups, coordination chemistry and growth direction.
If we conclude the observed data, we could say that spin coating results in a poly crystalline CoDHTA MOF thin film. The surface groups on the substrates appears to determine the growth direction of the crystals. We have observed a different growth on -OH terminated FTO glass compared to the -COOH terminated gold substrate. With IR we clearly see the coordination with the carboxylic acids and the hydroxide of the benzene. The AFM-IR results strongly indicate the formation of different coordination frameworks. It seems that for thin layers, the coordination direction is controlled by the surface groups. Chemical mapping of the benzene vibration at 1446-1460cm^{-1} can give insight in the type of coordination. It appears that the more the carbonyl coordinates to the cobalt, the lower the energy of the benzene ring vibration is.

4.3 CoATA

CoATA MOF thin films were prepared with spin coating on a MHDA functionalized gold substrate and FTO glass. As seen in the SEM image Figure 4.13c, CoATA appears as powder sugar. This was different compared to the structures of Co44BP and CoDHTA, although the preparation method was almost identical to that of CoDHTA. So, to first get an indication of the structural order of CoATA, XRD measurements were performed. In the right image of Figure 4.21 the XRD diffractograms are shown. For both substrates, broad peaks at 2θ positions 11.5°and 23.2°were observed. The broad peaks indicate that the samples contain no homogeneous oriented crystalline domains but an amorphous phase seems to have formed. To get more insight in the chemical bonds in the construction of this phase, IR and Raman measurements were performed.

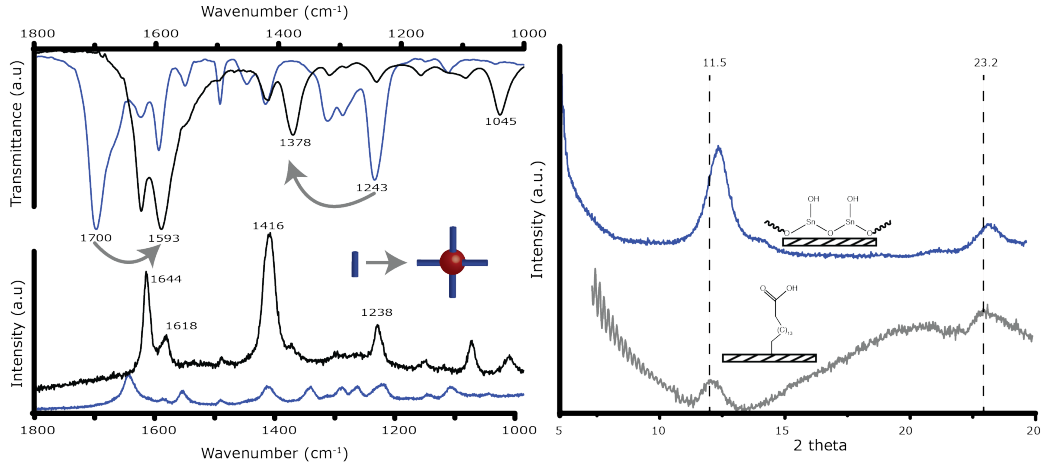

Figure 4.21: Left: IR (top) and Raman (bottom) spectra of ATA (blue) and CoATA (black). Right: XRD spectra of CoATA at MHDA and FTO glass surfaces.

In the left image of Figure 4.21, the IR and Raman spectra can be seen. The blue line represents the spectrum of ATA. The C=O and C-O stretching vibrations of the acid groups are clearly visible at 1243 and 1700 cm^{-1} respectively. The band at 1624cm^{-1} can be assigned to the N-H asymmetric bending vibrations. With the introduction of cobalt (II), the spectrum changes, black line. A band at 1378 cm^{-1} is introduced and the C=O stretching vibration has vanished. Moreover, The bands at 1593 cm^{-1} and 1624 cm^{-1} have broaden. A band at 1040 cm^{-1} was also observed. Tabulated IR data and DFT calculations were performed to identify and assign these bands. In Figure 4.22, the DFT-calculated IR spectra on two different possible coordination structures of ATA to cobalt (II) can be seen. The calculated spectra of ATA and CoATA are illustrated on the bottom part of the graphs and the measured spectra are present at the top part of the graphs.
In the left graph, the calculated IR spectrum of CoATA is shown where the amine group coordinates to the cobalt with the carbonyl group. The -OH group does not involve in the coordination. A shift in the C=O band can be observed starting at 1730 up to 1670 cm^{-1}. Because the calculations do not take into account the influence of external interactions, these bands should be interpreted as a general left shift of the carbonyl. These bands can be assigned to the C-O stretching vibrations of the

coordinating carbonyl: C-O—Co. Subsequently, the calculation showed that a strong band arises at 1384 cm^{-1}. According to DFT, these bands can be assigned to a C-C-OH vibration combined with a bending O-H vibration, as illustrated within the graph. This band almost exactly matches with the observed vibration at 1378 cm^{-1} for the measured CoATA. So, the calculated bands at 1730-1670 and 1378 cm^{-1} suggest that the acid is coupled to asymmetric and symmetric vibrations. However, this is not true here. Because the -OH group is not involved in the coordination, there is no symmetry between the two oxygen atoms of the acid. Without this symmetry, no coupling can occur. With this in mind, we could state that when the acid coordinates only with the carbonyl group to the cobalt, a new C-C-O-H vibration arises combined with a lower energetic C-O stretching vibration of the coordinating carbonyl.

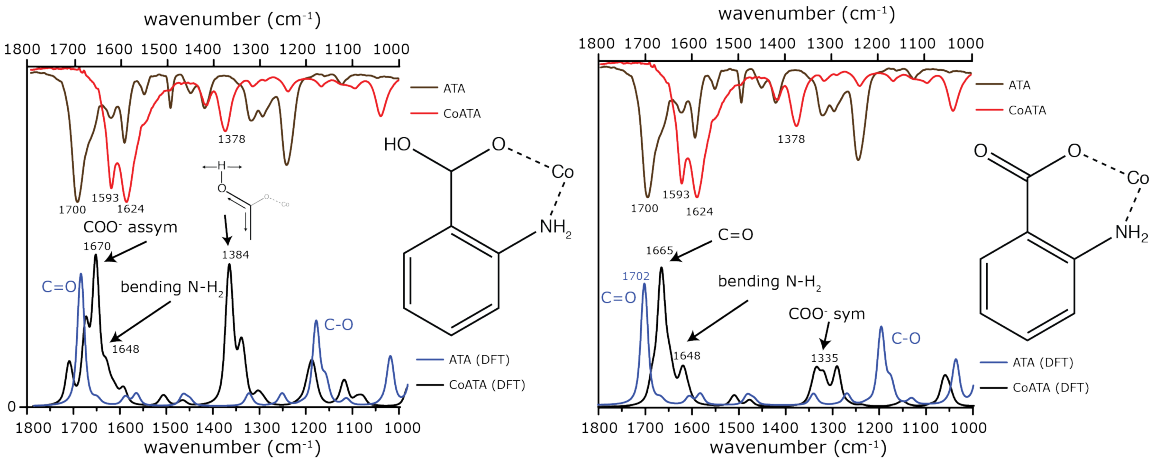

Figure 4.22: DFT results of CoATA for different coordinations. Bottom graphs are the calculated spectra of ATA (blue) and CoATA (black). The top graphs are the measured spectra of ATA (brown) and CoATA (red).

In the right graph, the calculated IR spectrum of CoATA is shown where the amine group coordinates to the cobalt with the deprotonated acid. The C=O group is not involved in the coordination. The calculations show that the C=O stretching vibration has shifted a little to lower energies. This indicates that electrons withdrawn from the bond (even though the bond is not involved in the coordination). A band at 1335 cm^{-1} arises and the calculation shown that this corresponds to a similar C-C-O stretching vibration as observed in the previous coordination. Again, there is no acid coupling in this type of coordination. We can conclude that, according to the DFT calculations, when the acid only partially coordinates to the cobalt(II), a C-C-O vibration in between 1300-1400 arises what is not the result of acid coupling. For the measured CoATA, this indicates that the bands at 1378 cm^{-1} and 1593 cm^{-1} do not specifically arises due to acid coupling. A partially coordinating acid results in the arising of bands in this energy region too. At least, according to the DFT calculations. So the point we learn here, is that the type of coordination cannot be studied by only looking to the IR vibrations of the acid groups. With Raman measurements however, the presence of symmetric vibrations can be monitored and can provide more insight in the type of coordinations. In the bottom graphs of the left image in Figure 4.21, the Raman spectra of ATA (blue line) and CoDHTA (black line) are presented. In the black line, a band at 1416 cm^{-1} arises. This band can be assigned to a symmetric C-O vibration. It

is unclear if this the COO^- symmetric stretching vibration of a coupled acid or an other kind of C-O symmetric stretching vibration, such as the latter described C-C-O vibration. It is difficult to assign this band to a specific vibration, but combined with the measured and calculated IR spectra, we could conclude that the acid is definitely involved in the coordination, but it is not clear yet what is the specific coordination.
To distinguish the two possible coordination structures described above, we should take a look at the O-H stretching vibrations. In Figure 4.23, the spectra of ATA (blue line) and CoATA (black line) in the energy region 4000-2000 cm^{-1} is shown. The characteristic O-H stretching band is observed in the region ±2800-3200. After the introduction of cobalt(II), this broad band was not present anymore.

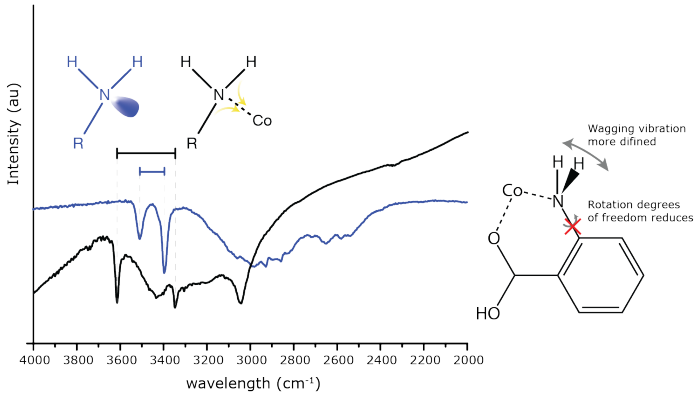

Figure 4.23: IR spectra of ATA (blue) and CoATA (black) between 4000-2000 cm^{-1}. The coordination to the amino group results in a reduction of the rotational degree of freedom.

This indicates that the acid was deprotonated but a new peak at ±3600cm^{-1} can be observed too. The energy of this peak is quite high and the only reasonable assignment of this peak is to a O-H stretching vibration. A sharp O-H stretching peak arises when the O-H group does not undergo hydrogen bonding. This could be the case when the O-H groups are located insight a crystal structure and are unable to create hydrogen bonds. The XRD measurements revealed that an amorphous phase was obtained after the synthesis. This means that there was not a crystalline phase present. The presence of free OH groups was therefore not the most likely. It may be that there were fractions of free OH groups in the pores of the amorphous material, but this is not certain yet. Furthermore, we observe two sharp peaks in the blue line between 3400-3600cm^{-1}. These are the asymmetric and symmetric N-H stretching vibrations of the amine. In the spectrum of CoATA, the peaks were not visible anymore in this energy region but two sharp peaks are present at ±3000 and ±3250 cm^{-1}. This indicates that the electronic environment of the nitrogen had changed. What exactly happened is not clear yet, but it strongly indicates that the amino groups were involved in the coordination to cobalt(II). To conclude this part, the IR, Raman and DFT analysis strongly indicate that both the acid (-OH and C=O) and the amine groups participate in the coordinate to cobalt (II). This resulted in an amorphous phase of CoATA on both MHDA and FTO surfaces.
To investigate if there were local irregularities at the surface, chemical mapping with AFM-IR was performed. The measurements were performed on CoATA@MHDA. In the left images of Figure 4.24, the AFM image is shown. The measurement showed that the topography of the surface was quite homogeneous. The difference in height lays around 100nm which is much more flat compared to

CoDHTA in Figure 4.20. At different points on the surface, an IR spectrum was taken. The right image in Figure 4.24 shows the corresponding IR spectra in the bottom of the graph. The top part of the graph represents the IR spectra of CoATA and ATA measured with IRRAS. The AFM-IR spectra are quite similar to the bulk spectrum of CoATA.

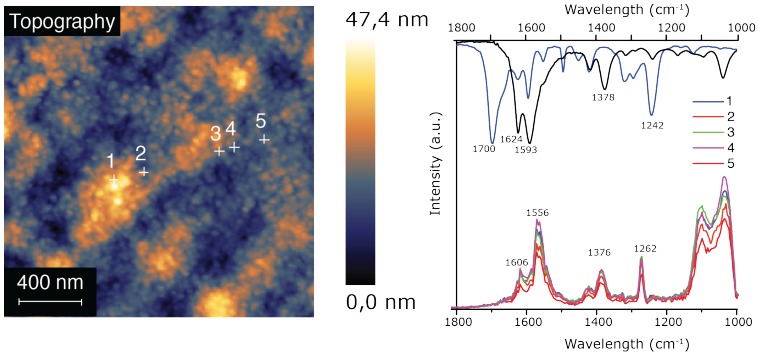

Figure 4.24: Left: AFM map of CoATA, Right: PiFM spectra (bottom) at different spots and IRRAS spectra (top) of ATA (blue) and CoATA (black)

The band in the IRRAS spectrum at 1593 cm^{-1}, however, seems to have shifted in the AFM-IR spectrum. This band is observed at 1556 cm^{-1}. It is not really clear why this band 'shifts' in the different IR techniques. In Appendix 2, chemical mapping of vibrations 1561 cm^{-1} (most probably COO^- asymm stretch) and 1378 cm^{-1} (most probably COO^- symm stretch) is presented. This mapping shows that the surface is chemically very homogeneous and almost no irregularities are observed for these chemical bonds. The intensity of the vibrations is very similar over the whole surface.
At another spot on the sample, a small irregularity is observed. A hiPYR map is measured on this spot with a resolution of 256x256 pixels. In Figure 4.25a, the AFM and hiPYR maps are shown. The high feature in the AFM image has a relatively low signal in the hiPYR map. This means a low IR signal is detected. To investigate what materials is located in this high feature, chemical maps at 1593 cm^{-1} and 1376 cm^{-1} were made, Figure 4.25b. It can be seen that both vibrations are significantly present and indicate the formation of a thin layer of amorphous CoATA. At the high feature, however, there is barely any signal of these vibrations. It appears that some other material is present there. After some analysis on the intensities of different vibrations over the entire spot surface, the vibration at 1450 cm^{-1} was the most intense at the high feature. The black line in Figure 4.25c represents the average IR signal of all the measured IR spectra on this spot. The blue line is a single IR spectrum taken on the high feature. We can see that it has some similarities, but the band at 1450 cm^{-1} is more intense compared to the black line. A band at 1450 cm^{-1} is typically an aromatic vibration. In the bulk IRRAS spectrum, Figure 4.21, a band at 1450 cm^{-1} is observed for pure ATA. It could be that some partially coordinated ATA is accumulated in this high feature. The word "partially" is chosen because no C=O stretching vibration is observed throughout the entire sample. For uncoordinated ATA this vibration should be present.
The main conclusion in the AFM-IR and XRD measurements is that the surface consists of a CoATA coating that is homogeneous in both height and chemical composition, and has an amorphous phase. The IR measurements and calculations strongly indicates that the amine groups of ATA coordinates to the cobalt (II) and creates, together with the carbonyl of the acid, a six membered ring. The -OH

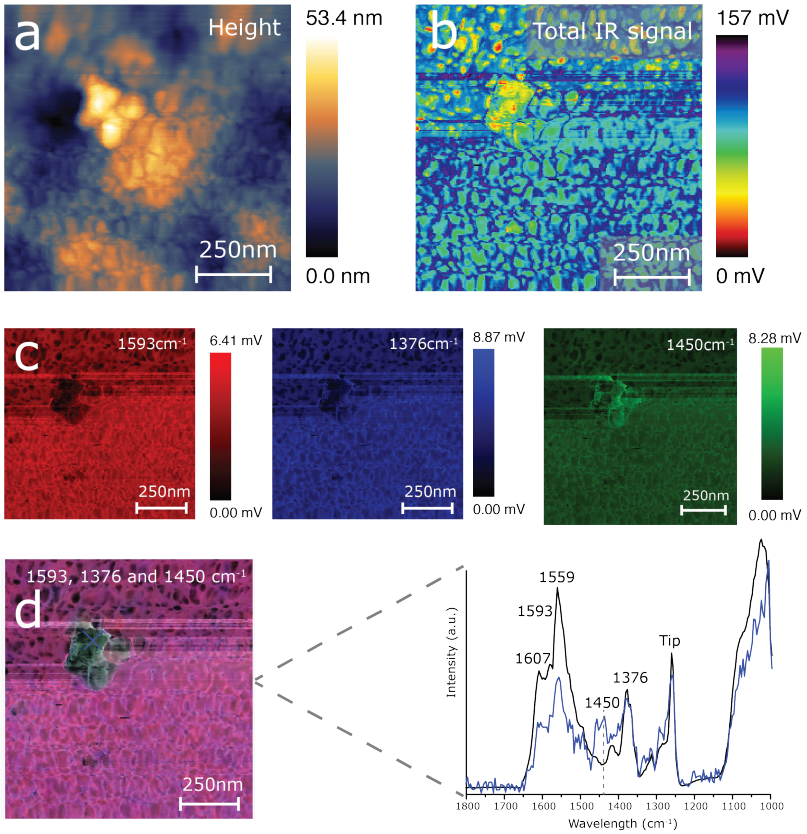

Figure 4.25: AFM-IR hyper results of CoATA. a) AFM tomography image. b) Total IR signal. The more blue the color, the higher the average signal. c) chemical mapping at vibrations 1593 cm^{-1} (COO^- asym), 1376 cm^{-1} (COO^- sym) and 1450 cm^{-1} (ring vibration). The colors correspond to the intensity of the signal. The brighter the color, the higher the signal. d) combined chemical maps and spectra of the average IR signal (black) and at the high feature (blue).

probably coordinates since it is not, or barely visible in the measured IR spectra. To get more insight in the electronical changes during the formation of CoATA, *in situ* UV-vis measurements during the growth were performed.

Monitoring solution growth

To get more insight into the origin of the coordination of ATA to the cobalt ions, *in situ.* (cuvet) liquid UV-vis measurements were performed. In these measurements the electronical changes of ATA can be monitored and provides information about the chemical environment of the different groups in ATA. In the left image of Figure 5.26 the electronic changes during the formation of CoATA in solution can be seen. The black line corresponds to pure ATA in ethanol. If we look in more detail to the nitrogen, we can see that the hybridization is sp^3. It is bound to two hydrogen atoms and a carbon from the benzene. This means that there is one lone pair remaining. The band at 365 nm was assigned to the $n \rightarrow \pi^*$ excitation, where 'n' is the lone pair of the nitrogen and π^* is the empty anti-bonding p orbital of the benzene. We see that, when cobalt(II) was introduced, this band starts to decrease. The degradation of this band indicates that the lone pair of the nitrogen was consumed. This supports the IR results along the formation of a nitrogen-cobalt coordination. We further observe a rising band at 310 cm^{-1}. This band is further described in the next chapter. To correlate the electronical changes to particle growth, dynamic light scattering (DLS) measurements were performed, Figure 5.26 right image.

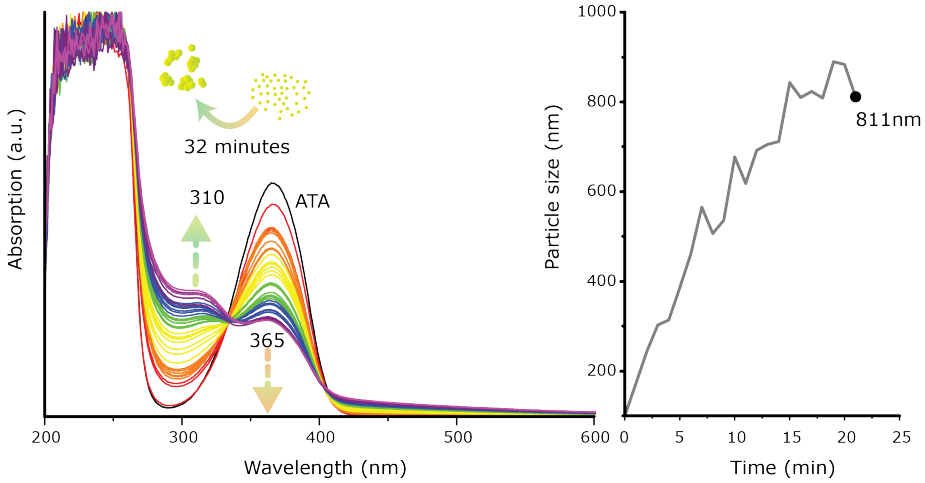

Figure 5.26: Right: *in situ* growth of CoATA. Every line represents one minute in time. After 32 minutes, the growth stagnated. Left: DLS measurements on the growth of cobalt (II) and ATA.

The measurements show that in 20 minutes, the MOFs grew up to ±800 nm (detection of the particles after 20 minutes was not accurate anymore due to the detection limit of the machine). It should be noted that the precursor parameter solutions for these measurements (UV-vis and DLS) differ with those for the synthesis of the MOF thin films. This was necessary to obtain accurate UV-vis and DLS measurements within the detection limits. The measurements give therefor a good indication for the electronic and geometric changes during the reaction but are not reliable on -scales. The DLS and UV-vis measurements show that the electronic structure of the organic linkers changes over time due

to the introduction of cobalt(II). Particles are formed and the degradation of the amine band at 365 nm suggest that the amino group is part of the coordination network of these particles.

The same experiment was performed with CoDHTA and Co44BP to compare if the growth differs with another linker. The black line in Figure 5.27 represents 4,4'bipyridine in ethanol. We have assigned the band at 240 nm to the $n \rightarrow \pi^*$ excitation, were 'n' is the lone pair of the nitrogen. Note that this electronic excitation is more blue shifted than the amino group of ATA. In 44BP, the nitrogen is more incorporated in a ring structure, and the lone pair will probably have a more p-orbital-type character. The excitation in the UV region is a logic result, since $pi \rightarrow pi^*$ excitations typical occur under UV illumination. When cobalt(II) was added to the solution, a similar trend as we saw during the growth of CoATA can be observed. The band at 240 nm reduces with increasing time. This indicates that the lone pair of the nitrogen was consumed over time. This is a convincing consequence, since the nitrogen coordinates to the cobalt. This result strengthens the argument that the amino group of ATA could indeed coordinate to the cobalt(II) ion. For Co44BP, no DLS measurements were performed. Co44BP thin films were made with LbL synthesis and do not relay on particle growth in solution. This UV-vis experiment was only performed to show that the same phenomena occurred with another organic linker containing a nitrogen.

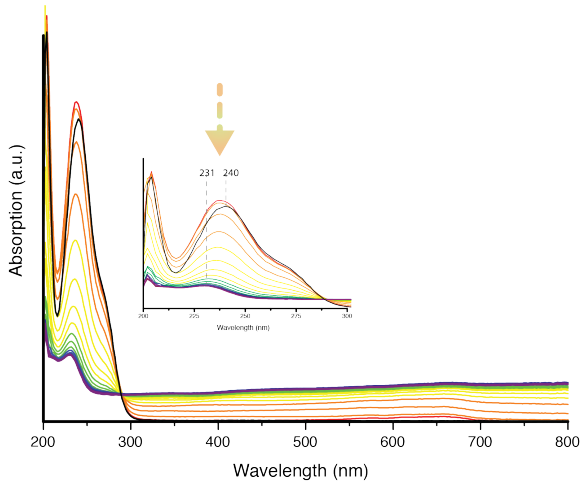

Figure 5.27: *in situ* growth of Co44BP. Every line represents one minute.

For CoDHTA, we do not see the same phenomenon during the growth, Figure 5.28 left image. Again, the black line represents DHTA. The band at 374 nm was assigned to the lone pairs of the hydroxide oxygen atoms attached to the benzene ring, $n \rightarrow \pi^*$. When cobalt (II) was introduced, the band slightly shifts to the left. After 4 minutes however, the band starts to broaden, and shifts to the right. We hypothesize that the electronic structure of the OH groups changes combined with a formation of an new electric system. This is similar to CoATA and is discussed in the next chapter too. The DLS measurements show that CoDHTA particles grow almost twice as fast compared to CoATA, Figure 5.28 right image. The XRD measurements showed that crystalline CoDHTA thin films were obtained and amorphous CoATA films. the CoDHTA particles could probably grow much faster because it forms this coordination polymer network in a certain direction. For CoATA, the particles grew probably in

random directions and form amorphous structures. This could result in stagnation of the growth due to a defect in the coordination network and causes slower particle growth.

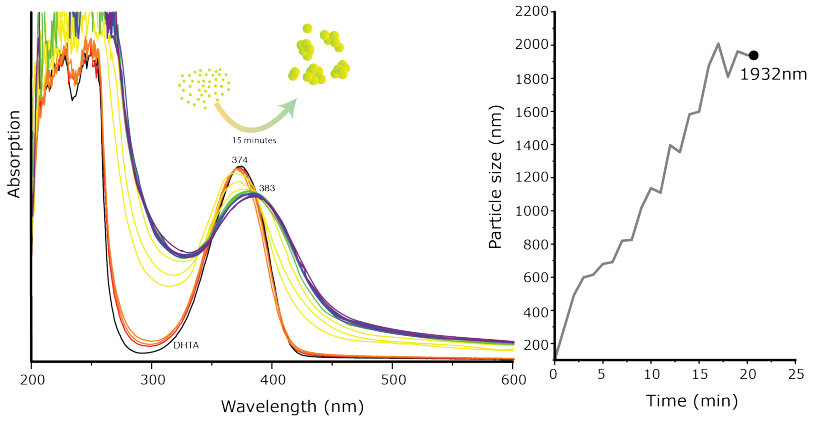

Figure 5.28: Right: *in situ* growth of CoDHTA. Every line represents one minute. Left: DLS measurements on the growth of cobalt(II) and DHTA.

The growth is not only controlled by time but the molar ratio between the linker and the metal ion has an influence as well. Figure 5.29 shows the absorption spectra between 200-300 nm of varied ratios of cobalt acetate and ATA and DHTA mixtures after 1 hour. Focusing on CoDHTA, for the molar ratio's where DHTA is equal or higher in concentration compared to cobalt(II), bands at 252 and 220 nm were observed. These bands can be assigned to the $n \rightarrow \pi^*$ transition of the (aromatic) carboxylic acids. We can see that when an excess of linker was used, these absorption bands remain visible. This indicates that the linker is still present in the solution and not consumed in the metal organic framework.

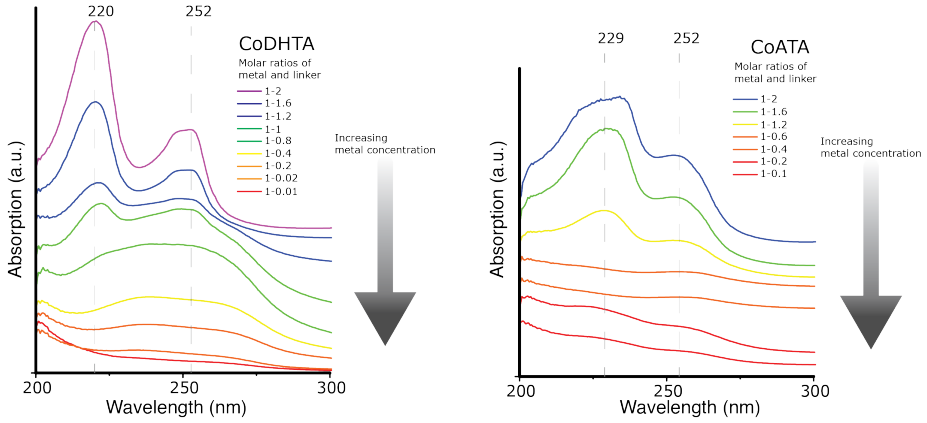

Figure 5.29: UV-vis measurements on different ratio's metal to linker on CoDHTA and CoATA.

With reducing linker concentration however, the absorption bands started to decrease too. The bands

as 252 and 220 nm disappears and a brought band between 300 and 200 nm appears. This indicates that the electronic composition of the acid groups has changed which is in agreement with the coordination of cobalt to the acid groups of DHTA. With the data from Figure 5.28 we could conclude that it strongly indicates that both acid and hydroxide groups coordinate to the cobalt.
We now apply this knowledge to the spectra of CoATA. With elevated concentrations of ATA we can observe acid $n \rightarrow \pi^*$ transitions at 252 and 229 nm. An interesting observation is that with decreasing ATA concentration, these bands still remain visible. This result suggests that the electronic structure of the acid (partially) remains constant with increasing Co(II):ATA ratios. This indicates that the acid groups of ATA do not coordinate completely to the cobalt. The band at 229 nm, however, decreases compared to the band at 252 nm. We can now state that maybe one part of the acid coordinates to the cobalt, (for example the carbonyl group) and in all probability along with the nitrogen. This is something that was concluded in the IR measurements as well.
So to conclude the structural analysis, we could say that it appears that ATA coordinates to the cobalt(II) with both the acid groups and the amino groups but in a random order. The measurements strongly indicate that the acid does not always completely coordinates to the cobalt(II). For CoDHTA, the coordination most certainly involves both the acid and hydroxide groups and creates crystalline coordination networks.

Light harvesting and exciton formation

After the structural analysis, the light harvesting properties and exciton formation performance of Co44BP, CoDHTA and CoATA thin films where exploited with diffusive reflectance UV-vis spectroscopy (DRUV-vis) and transient absorption spectroscopy (TAS). The dip coater broke during this theses and Co44BP thin films could not be prepared. The DRUV-vis of Co44BP are not included in this chapter. The diffusive reflectance was measurement for MOF thin films grown on FTO glass.

6.1 Diffusive reflection UV-vis of CoDHTA and CoATA on FTO

In the left image of Figure 6.30 the DRUV-vis spectra of different layers of CoDHTA@FTO are presented. The dashed gray line represents the DRUV-vis signal of bare FTO glass. In the right image, the DRUV-vis of the bulk powder can been seen. With increasing layers of CoDHTA on the FTO glass, the band at 383 nm increases. In the previous chapter, this band was observed as well during the growth of CoDHTA in solution, see figure 5.28 on page 37. This band is the result of the reaction between cobalt and DHTA. To assign this band to a certain excitation, a few comments should be made. First of all, the $n \rightarrow \pi^*$ excitation of the oxygen in the hydroxide group, to the anti bonding p-orbitals of the benzene occurs at the same energies region (at 374 nm). This excitation however, results in a more sharp band, as observed in the previous chapter. The LMCT of acid coordinated cobalt in cobalt terephthalic-acid MOFs, occurs at around 350 nm as described by Abbasi *et al.* [50]. So, in all probability, the band at 382 nm could be the result of the LMCT Co-O overlapping with the $n \rightarrow \pi^*$ excitation within DHTA.

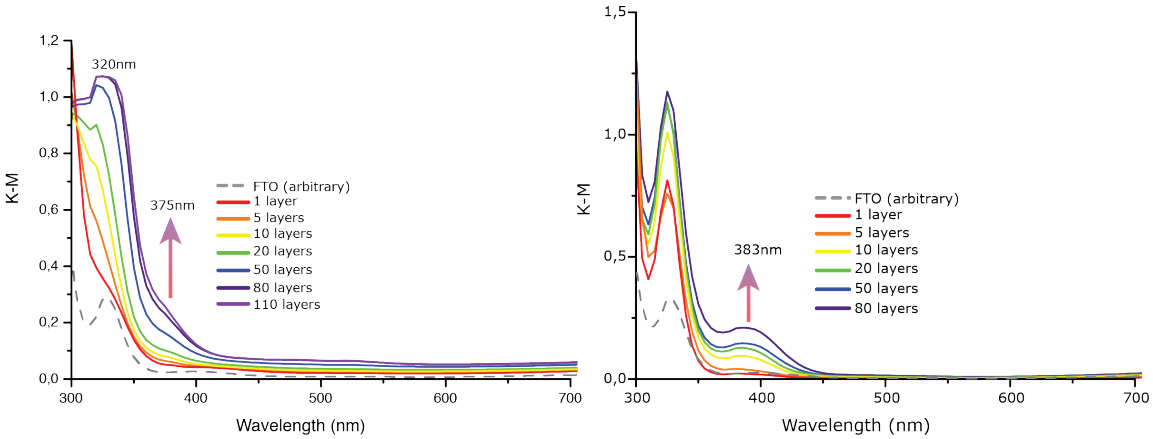

Figure 6.30: DRUV-vis spectra of left: CoDHTA@FTO and right: CoATA@FTO

For CoATA@FTO, a band at 375 nm arises with increasing layer thickness, right image in Figure 6.30. This is a very similar phenomenon to the CoDHTA spectra. Due to the similarities between the molecule structure of ATA and DHTA we could argue that this band corresponds to the LMCT as well. The paper of Abbasi *et al.* describes that the LMCT of Co-N and C-O both both occur at 350 nm. It is therefore difficult to distinguish if the C0-N or C0-O are observed here.
The position of the LMCT versus standard hydrogen potential was not determined. A possible route for the determination of this is presented in the outlook.

6.2 Transient Absorption Spectroscopy of CoDHTA and Co44BP

Transient absorption spectroscopy (TAS) was applied to study the lifetime of the excited states in the SURMOFs. The corresponding half-life times are obtained by using kinetic models with different consecutively decaying state that fit the observed transients.

Regarding CoDHTA, left image of Figure 6.31, a transient kinetic model with two consecutively decaying states was necessary to obtain a good fit for the experimental data. We observed an adsorption peak at 518 nm followed by a continuous adsorption band up to 700 nm. The drop in adsorption at 533 nm was light contamination and should not be considered as a valid data point. Under 500 nm, a negative δA represents bleaching of the ground state. This indicates that the ground state carriers were depleted to excited states. For the negative peak, two half-life times are found: 2,5ns (91%) and 141ns (9%). The percentage of these times are obtained by the kinetic model. Subsequently two half-life times were associated to the peak at 518 nm: 1,972ns (91%) and 24,5ns (9%). The presents of multiple life times indicates that the relaxation of the excited state probably occurs via multiple routes. The percentages give an indication which relaxation route occurs the most. Here, it appears that most excited stages relax back in a few nano seconds. But for a small fraction (9%) it appears that it takes longer to relax back to the ground state. As illustrated in figure 6.32, multiple relaxation routes could occur after excitation. For the fast relaxations (in the order of nano seconds), the relaxation could perhaps simply be the same way as the excitation occurred. But if the excited electron is somehow trapped in another energy lever, the relaxation of the electron could take longer.

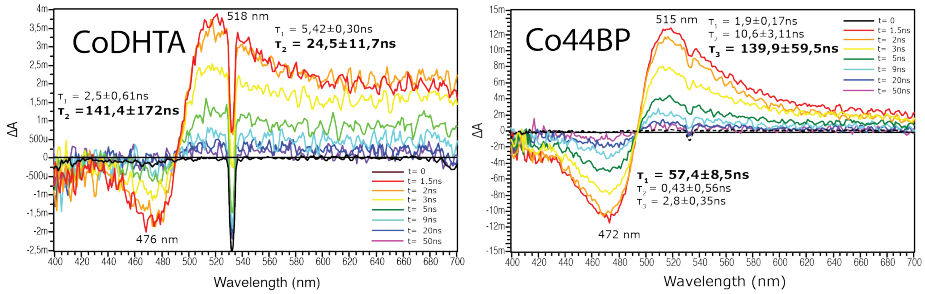

Figure 6.31: Transient absorption spectra of a) CoDHTA@MHDA and b) Co44BP@MHDA.

With this TAS data alone, it is difficult to determine the origin of these transients and relaxation half-life times. Nevertheless, a few hypotheses are discussed.
As described in the experimental section, a 265 nm laser was used to excite the sample. This energy is higher than the estimated LMCT for CoDHTA. The transients could therefore be originating from

the excitation and relaxation of the LMCT. The different time scales suggest that relaxation of the excited stages to the ground state has multiple routes, as schematically illustrated in Figure 6.32. The long lifetimes, in the order of 10^2 ns, could be promising for photo catalysis because CO_2 reduction reactions typically occur in micro seconds [51].
The transients could also be induced by the d-d excitation and relaxations. The d-d transitions absorb light between 450 and 600 nm [52, 53]. This energy region corresponds to the observed transients . It is however difficult to defend this, with only this data. More TAS analysis on cobalt (II) should be performed to strengthen these arguments.

TAS measurements on Co44BP resulted in similar TAS spectra, see Figure 6.31b. A depletion of the ground state is observed around 472 nm and an absorption at 515 nm. This is very similar to CoDHTA and rises some questions. The organic linkers 44BP and DHTA, do not have similar chemical properties. 44BP consist of two coupled pyridine rings and coordinate with the nitrogen to the cobalt while the acid and hydroxide groups of DHTA coordinate to cobalt. With this in mind, the argument that these transients resulted from d-d transitions is reinforced.
In a last option, which has not be discussed yet, the transients could rise from multiple origins. The d-d and LMCT transitions could be coupled in a complex electronic way. The explanation of the specific origin of these transients could be very important for the analysis and further improvement for the cobalt thin films but is beyond the scope of this thesis.

Unfortunately, no transients were observed for CoATA. We do not know for sure whether this is because the measurement was not successful, or that CoATA can not induce transients. More TAS analysis should be performed.

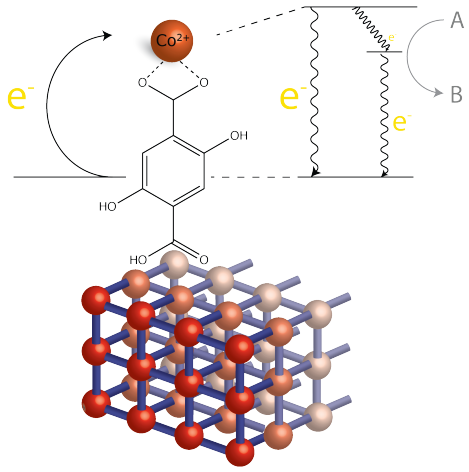

Figure 6.32: Schematic illustration LMCT excitation. After excitation of the linker the relaxation could occur in different ways. First, it could intermediately relax back to the ground state. On the other hand, the relaxation could occur in different steps. The electron could be trapped in an energy state before it completely relaxes back. This will take a longer time than when it relaxes back at once. Life times of the electrons are preferred for catalysis.

Catalytic testing

7.1 CO_2 photo-reduction

The main goal of this thesis was to prepare and investigate cobalt-based MOF thin films for the photo-reduction of CO_2. With the previous analysis and observations, CoDHTA@FTO was chosen for catalytic experiments. This MOF thin film was crystalline and showed potential in light harvesting and exciton formation. The first attempts for the photo-reduction of CO_2 using CoDHTA did however not result in any product formation. Some CO and CH_4 gasses were detected in the start of the reaction but their presence reduced over time. These gasses were probably present due to either contamination of the reduction setup or destruction of the CoDHTA framework. Because the time of this thesis was running out and the assistance and availability for the photo-catalytic reaction setup was limited, no other photo-catalytic experiments were performed. In stead, the electrochemical reduction performance of CoDHTA@FTO was investigate to see if the MOF thin films as any potential towards catalysis.

7.2 Electrochemical reduction of Methylene blue

For the electrochemical reduction performance, the degradation of methylene blue (MB) was performed. Recall that in this reaction, see Figure 3.11, the -N=C- group of the thiazine is reduced to a -NH-CH- group. This requires two hydrogen atoms and two electrons. Hydrogen peroxide (H_2O_2) was used as oxidation agent. In this processes, the catalytic performance of CoDHTA@FTO to accelerate the reduction of MB was investigated.
Before the catalytic measurements, the reaction between H_2O_2 and MB without a catalyst was investigated. In Figure 7.33a, the UV-vis measurements (between 500-700 nm) on the degradation of MB is shown. The black line represents the electronic bands of MB in ethanol without hydrogen peroxide. We can see that after 255 minutes, almost no MB had been reduced. The absorbance was reduced by only $\pm.0.19$. This suggest that under these conditions, almost no reaction occurs.

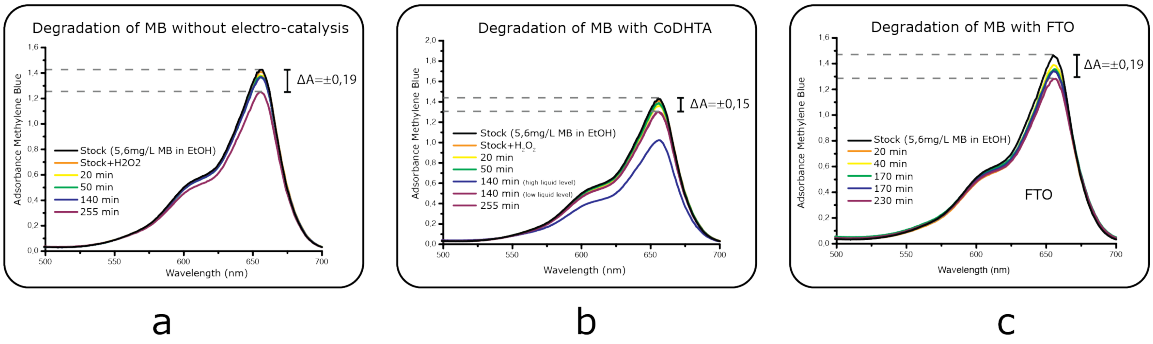

Figure 7.33: UV-vis spectra of the degradation of MB in ethanol with a) only FTO as catalyst, b) CoDHTA@FTO as catalyst, c) no catalyst. In all reactions, H_2O_2 was used as oxidative agent.

The first measurements on the electro-catalytic reduction were performed using transient voltammetry. A constant potential was applied between the catalyst and the counter electrode and the induced current was measured over time. Unfortunately, almost no current (±10nA) was observed for potentials up to -4V.
Alternatively, the catalytic performance was tested using transient potentiometry (TP). In this method, a constant electric current was applied on the catalyst. The main idea of this method was to test how well the catalyst, CoDHTA@FTO, was able to transport these electrons to the reactants.

In Figure 7.34a, the TP measurement on CoDHTA@FTO under MB reduction conditions is shown. We can see that in the first 100 minutes, the measured potential on the reaction was fluctuating and lies around -1,4V. After this, the potential takes over a more constant value around -1,20, -1,30V. The sudden drops in potential are due to the sample collection of the reaction mixture.

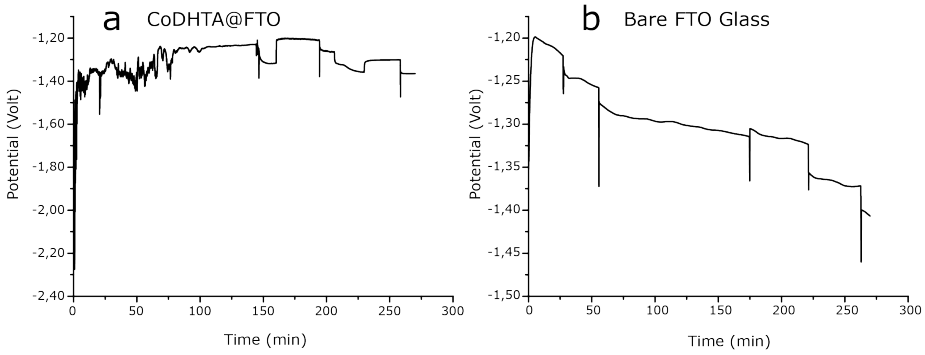

Figure 7.34: Potential measurements over time on a) CoDHTA@FTO and b) bare FTO glass with a constant current of 100μA.

In Figure 7.33b, the UV-vis measurements of the degradation of MB under catalysis of CoDHTA@FTO is shown. Again, the black line represents the absorbance spectrum of MB in ethanol. We can see that after the first 50 minutes (green line), almost nothing had happened. The absorbance was almost equal to the initial band. During the reaction however the upper layer of the reaction solution started to became transparent, while the rest of the mixture was still blue colored by the MB. A sample of the upper and bottom layer of the mixture was taken and measured with UV-vis. The difference in absorbance can clearly be observed. In the upper layer (blue line), less MB was present compared to the bottom layer (purple line). Recall from the methodology section, the catalyst side was present in the upper layer of the solution. There is no clear conclusion about what causes these observations. With optical microscopy the surface of the FTO glass was pictured before and after catalysis, Figure 7.35.
Before catalysis, the surface consists of the characteristic needle-like crystals. After the reaction however, no clear structure was observed. This indicated that the CoDHTA crystals are destroyed during the reaction. The fluctuating potential observed in Figure 7.34a could be the result the MOF that was slowly falling apart. The observed transparent solution could be caused by the demolishing of the catalyst. The products resulting from that could maybe somehow causes a diffusion of the MB to the lower part of the reactor. After this observation, the mixture was stirred by gently bubbling

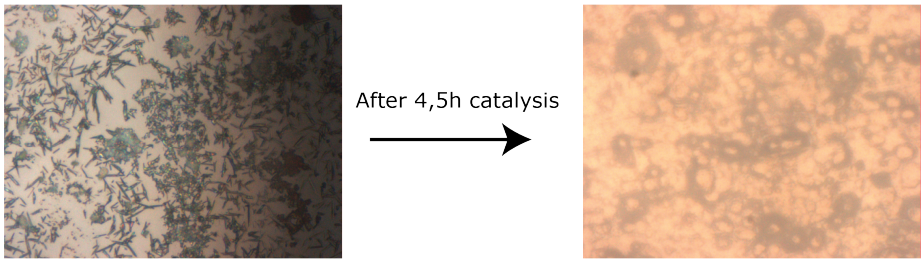

Figure 7.35: Optical microscopy images of CoDHTA@FTO before and after catalysis. After the catalysis, the surface is completely different and it appears that the MOF is destroyed.

some argon in the solution (20ml/min). and the absorbance of MB was measured again. As one can see in Figure 7.33b, the total amount of MB in the solution had not significantly reduced. No hard conclusions on these phenomena could be made so far.

Finally, to complete this small catalytic study, the influence of FTO glass was investigated. Similar UV-vis results are obtained, Figure 7.33c. Within the same time, a similar amount of MB had been reduced. In Figure 7.34, the TP measurements on bare FTO glass is illustrated. We observe similar potentials over time compared to CoDHTA@FTO. Again, the sudden drops in potential are due to sample collection. We can see that the potential drops. Although it is quite difficult to give a good explanation for this, based on only the data on potentials, some hypothesis could be made. Potentiometry measurements relay on an oxidation reaction at the cathode and a reduction reaction on the anode (recall methodology section). Next to MB, H_2O_2 was present in the solution. We could argue that, with an given constant current, H_2O_2 can be oxidized and reduced respectively on the cathode and anode. With increasing time, the amount of H_2O_2 reduces and the potential required to maintain 100μA increases.
To conclude this part, we see that the reduction of MB was barely improved using CoDHTA@FTO as catalyst. The reaction time did not increase. The MOF thin film was not stable in the reaction conditions and was destroyed.

Conclusions

In this thesis the synthesis, characterization and catalytic testing of cobalt based metal organic framework thin films have been described. The Co44BP thin films were prepared by using a layer by layer synthesis approach. IR and Raman measurements indicated that 44BP was coordinated to cobalt(II) and the formation of a crystalline product was confirmed by XRD measurements. On all the substrates, FTO and gold substrates functionalized with 16-mercaptohexadecanoic acid (MHDA) and 4-mercaptopyridine, the crystallinity was identical suggesting that on these substrates, the growth of the MOF crystal was independent of the surface groups. The distribution of the 44BP crystals over the surface was investigated with ToF SIMS analysis and the measurements showed that the Co44BP framework was homogeneously distributed.
Spin coating of a CoDHTA dispersion on FTO and MDHA surfaces resulted in poly-crystalline thin films. The crystals anchored on the surface ranged in sizes from monolayers to micrometer sized crystals. XRD measurements revealed different crystalline domains for CoDHTA@FTO and CoDHTA@MHDA. The IR, Raman and PiFM analyses indicated that the preferred orientation of the crystals depended on the surface groups of the substrate. A hypothesis is that with a -OH terminated surface, the direction of the CoDHTA crystals could be in-plane with the OH groups of DHTA. Whereas for -OOH terminated surfaces, the crystals could be in-plane with the acid groups of DHTA. XRD measurements on very thin layers of CoDHTA on the different substrates should however be performed to strengthen this hypothesis. AFM analysis combined with DFT calculations have shown that different coordination structures were present on both surfaces. It appears that the higher features on the surface have a different coordination network than the thin films. Spin coating of CoATA resulted in an amorphous thin film as observed in the XRD measurements. The IR, Raman,and DFT analyses showed that ATA coordinated with both the acid and the hydroxide groups. This was also confirmed by the *in situ* UV-vis measurements. The AFM-IR measurements showed a very homogeneous distribution of the CoATA film over the surface with almost no irregularities.
Regarding the light harvesting properties, the ligand to metal charge transfer for CoDHTA and CoATA was observed at 383 and 375 nm respectively. The position of these LMCT versus the SHE was not obtained be could provide more insight in the catalytic potential for these MOFs and is further described in the outlook. Transient absorption spectroscopy revealed transients for both Co44BP and CoDHTA. Both transients were very similar and it is therefore difficult to determine their origins. The transients could either be induced by d-d transitions or by LMCT events. In both cases, the half-life times of the transients are low for CO_2 photo reduction. The maximum half-life times for Co44BP and CoDHTA were respectively 139 $\pm$59,5ns and 141,4$\pm$172ns.
No activity in the photo-reduction of CO_2 was observed. Some CO and CH_4 gasses were detected but it is doubtful if these were reaction products. Catalytic experiments on the electrochemical reduction of methylene blue (MB) with CoDHTA@FTO using H_2O_2 did not show any improved activity. The reaction with or without catalyst showed no significant difference. A strange transparent layer on top of the reaction mixture was observed and did only occur when CoDHTA was used as catalyst. A decrease in concentration MB was observed in this layer. It is still unclear what causes this. The optical images revealed that the CoDHTA coating was destroyed. Perhaps, this could have resulted in diffusion of MB to lower areas in the reactor but a good explanation is as yet not available.

Outlook

This outlook describes possible research routes to improve and extend the work presented in this thesis.

9.1 Structural analysis

To get more insight into the position and oxidation state of the cobalt in the MOF thin films, X-ray photoelectron spectroscopy (XPS) could be performed. In this technique, X-rays are irradiated on a surface and electrons in the atoms escape from their shell. The electrons are detected in the detector and their kinetic energy is determined. When the electrons are detected, not only the position of the metal can be determined but the elements bound to the metal can be analyzed as well. For CoDHTA and CoATA, this could be very interesting: to really map the type of coordination we have discussed in this thesis.

This technique could also be interesting to use for the analysis of multivariate MOFs: MOFs with multiple organic linkers. The introduction of two organic linkers to cobalt brings complexity, and asks for accurate analyses from different perspectives. In Appendix 3, preliminary results of a multivariate cobalt(II) MOF are presented.

9.2 Determination of LMCT position

With DRUV, the energy of the LMCT was obtained for CoDHTA and CoATA. To determine at what energy position this transfer occurs compared to the standard hydrogen electrode (SHE), the MOFs could be incorporated in a photovoltaic cell, as described by Alvaro *et al.* [54]. The position can be determined by measuring the open circuit voltage and compare this to an other photovoltaic cell with a material that has a known LMCT/bandgap position. The best known photovoltaic cell for this purposes is titania. The difference in potential energy (volts) between the MOF and the titania will give an indication of the LMCT position versus SHE. In Appendix 4, preliminary results on the construction of a photovoltaic cell with CoDHTA is presented.

9.3 Catalytic testing

In this project, little research on the catalytic performance of the MOFs was done. More experiments on the stability and activity of the reducing capabilities of CoDHTA should be performed. This could be done by investigating the CO_2 photo-reduction capacities but it can also be performed on CO reduction. This lowers the energy barrier because it avoids the formation of the intermediate $CO_2{}^{-}{}^{*}$. The catalytic performance of CoATA should also be tested. Although CoATA formed an amorphous phase, that does not mean that it has no potential in catalysis.

Bibliography

[1] H. Furukawa, K. E. Cordova, M. O'Keeffe, and O. M. Yaghi, "The chemistry and applications of metal-organic frameworks," *Science*, vol. 341, no. 6149, pp. 974–987, 2013.

[2] Y. R. Lee, J. Kim, and W. S. Ahn, "Synthesis of metal-organic frameworks: A mini review," *Korean Journal of Chemical Engineering*, vol. 30, no. 9, pp. 1667–1680, 2013.

[3] H. Li, K. Wang, Y. Sun, C. T. Lollar, J. Li, and H. C. Zhou, "Recent advances in gas storage and separation using metal–organic frameworks," *Materials Today*, vol. 21, no. 2, pp. 108–121, 2018.

[4] L. E. Kreno, K. Leong, O. K. Farha, M. Allendorf, R. P. Van Duyne, and J. T. Hupp, "Metal-organic framework materials as chemical sensors," *Chemical Reviews*, vol. 112, no. 2, pp. 1105–1125, 2012.

[5] A. Dhakshinamoorthy, Z. Li, and H. Garcia, "Catalysis and photocatalysis by metal organic frameworks," *Chemical Society Reviews*, vol. 47, no. 22, pp. 8134–8172, 2018.

[6] D. Zacher, O. Shekhah, C. Wöll, and R. A. Fischer, "Thin films of metal-organic frameworks," *Chemical Society Reviews*, vol. 38, no. 5, pp. 1418–1429, 2009.

[7] A. Bétard and R. A. Fischer, "Metal-organic framework thin films: From fundamentals to applications," *Chemical Reviews*, vol. 112, no. 2, pp. 1055–1083, 2012.

[8] O. Shekhah, J. Liu, R. A. Fischer, and C. Wöll, "MOF thin films: Existing and future applications," *Chemical Society Reviews*, vol. 40, no. 2, pp. 1081–1106, 2011.

[9] K. A. Ali, A. Z. Abdullah, and A. R. Mohamed, "Recent development in catalytic technologies for methanol synthesis from renewable sources: A critical review," *Renewable and Sustainable Energy Reviews*, vol. 44, pp. 508–518, 2015.

[10] Z. Jiang, T. Xiao, V. L. Kuznetsov, and P. P. Edwards, "Turning carbon dioxide into fuel," *Philosophical Transactions of the Royal Society A*, vol. 368, no. 1923, pp. 3343–3364, 2010.

[11] S. Wang, W. Yao, J. Lin, Z. Ding, and X. Wang, "Cobalt imidazolate metal-organic frameworks photosplit CO2 under mild reaction conditions," *Angewandte Chemie - International Edition*, vol. 53, no. 4, pp. 1034–1038, 2014.

[12] B. Fisher and R. Eisenberg, "Electrocatalytic Reduction of Carbon Dioxide by Using Macrocycles of Nickel and Cobalt," *Journal of the American Chemical Society*, vol. 102, no. 24, pp. 7361–7363, 1980.

[13] Y. Lee, S. Kim, J. K. Kang, and S. M. Cohen, "Photocatalytic CO2reduction by a mixed metal (Zr/Ti), mixed ligand metal-organic framework under visible light irradiation," *Chemical Communications*, vol. 51, no. 26, pp. 5735–5738, 2015.

[14] C. Palomino Cabello, G. Gómez-Pozuelo, M. Opanasenko, P. Nachtigall, and J. Čejka, "Metal–Organic Frameworks M-MOF-74 and M-MIL-100: Comparison of Textural, Acidic, and Catalytic Properties," *ChemPlusChem*, vol. 81, no. 8, pp. 828–835, 2016.

[15] M. J. Kalmutzki, N. Hanikel, and O. M. Yaghi, "Secondary building units as the turning point in the development of the reticular chemistry of MOFs," *Science Advances*, vol. 4, no. 10, p. 9180, 2018.

[16] T. D. Bennett and A. K. Cheetham, "Amorphous metal-organic frameworks," *Accounts of Chemical Research*, vol. 47, no. 5, pp. 1555–1562, 2014.

[17] A. L. Linsebigler, G. Lu, and J. T. Yates, "Photocatalysis on TiO2 Surfaces: Principles, Mechanisms, and Selected Results," Tech. Rep. 3, 1995.

[18] R. Saravanan, F. Gracia, and A. Stephen, *Nanocomposites for Visible Light-induced Photocatalysis*. 2017.

[19] A. Sathrum, C. P. Kubiak, B. Kumar, T. Dang, J. Froehlich, and M. Llorente, " Photochemical and Photoelectrochemical Reduction of CO 2 ," *Annual Review of Physical Chemistry*, vol. 63, no. 1, pp. 541–569, 2012.

[20] X. Chang, T. Wang, and J. Gong, "CO2 photo-reduction: Insights into CO2 activation and reaction on surfaces of photocatalysts," *Energy and Environmental Science*, vol. 9, no. 7, pp. 2177–2196, 2016.

[21] D.-M. Feng, Y.-P. Zhu, P. Chen, and T.-Y. Ma, "Recent Advances in Transition-Metal-Mediated Electrocatalytic CO2 Reduction: From Homogeneous to Heterogeneous Systems," *Catalysts*, vol. 7, no. 12, p. 373, 2017.

[22] I. I. Alkhatib, C. Garlisi, M. Pagliaro, K. Al-Ali, and G. Palmisano, "Metal-organic frameworks for photocatalytic CO2 reduction under visible radiation: A review of strategies and applications," 2018.

[23] D. S. A. Simakov, *Electrocatalytic Reduction of CO2*. 2017.

[24] D. Li, S. Wang, J. Wang, X. Zhang, and S. Liu, "Synthesis of CdTe/TiO2 nanoparticles and their photocatalytic activity," *Elsevier*, vol. 48, no. 10, pp. 4283–4286, 2013.

[25] T. B. Nguyen and R. A. Doong, "Fabrication of highly visible-light-responsive ZnFe2O4/TiO2 heterostructures for the enhanced photocatalytic degradation of organic dyes," *RSC Advances*, vol. 6, no. 105, pp. 103428–103437, 2016.

[26] Https://www.visionlearning.com, "Factors that control Earth's temperature," 2016.

[27] M. A. Nasalevich, M. Van Der Veen, F. Kapteijn, and J. Gascon, "Metal-organic frameworks as heterogeneous photocatalysts: Advantages and challenges," *CrystEngComm*, vol. 16, no. 23, pp. 4919–4926, 2014.

[28] G. Givaja, P. Amo-Ochoa, C. J. Gómez-García, and F. Zamora, "Electrical conductive coordination polymers," *Chemical Society Reviews*, vol. 41, no. 1, pp. 115–147, 2012.

[29] C. Wang, D. Liu, and W. Lin, "Metal-organic frameworks as a tunable platform for designing functional molecular materials," *Journal of the American Chemical Society*, vol. 135, no. 36, pp. 13222–13234, 2013.

[30] M. A. Nasalevich, M. Van Der Veen, F. Kapteijn, and J. Gascon, "Metal-organic frameworks as heterogeneous photocatalysts: Advantages and challenges," *CrystEngComm*, vol. 16, no. 23, pp. 4919–4926, 2014.

[31] M. A. Nasalevich, M. G. Goesten, T. J. Savenije, F. Kapteijn, and J. Gascon, "Enhancing optical absorption of metal-organic frameworks for improved visible light photocatalysis," *Chemical Communications*, vol. 49, no. 90, pp. 10575–10577, 2013.

[32] Y. Zheng and S. Z. Qiao, "Direct Growth of Well-Aligned MOF Arrays onto Various Substrates," *Chem*, vol. 2, no. 6, pp. 751–752, 2017.

[33] H. Q. Xu, K. Wang, M. Ding, D. Feng, H. L. Jiang, and H. C. Zhou, "Seed-Mediated Synthesis of Metal-Organic Frameworks," *Journal of the American Chemical Society*, vol. 138, no. 16, pp. 5316–5320, 2016.

[34] W. J. Li, M. Tu, R. Cao, and R. A. Fischer, "Metal-organic framework thin films: Electrochemical fabrication techniques and corresponding applications & perspectives," *Journal of Materials Chemistry A*, vol. 4, no. 32, pp. 12356–12369, 2016.

[35] M. L. Ohnsorg, C. K. Beaudoin, and M. E. Anderson, "Fundamentals of MOF Thin Film Growth via Liquid-Phase Epitaxy: Investigating the Initiation of Deposition and the Influence of Temperature," *Langmuir*, vol. 31, no. 22, pp. 6114–6121, 2015.

[36] V. Chernikova, O. Shekhah, and M. Eddaoudi, "Advanced Fabrication Method for the Preparation of MOF Thin Films: Liquid-Phase Epitaxy Approach Meets Spin Coating Method," *ACS Applied Materials and Interfaces*, vol. 8, no. 31, pp. 20459–20464, 2016.

[37] J. Benito, S. Sorribas, I. Lucas, J. Coronas, and I. Gascon, "Langmuir-Blodgett Films of the Metal-Organic Framework MIL-101(Cr): Preparation, Characterization, and CO2 Adsorption Study Using a QCM-Based Setup," *ACS Applied Materials and Interfaces*, vol. 8, no. 25, pp. 16486–16492, 2016.

[38] J. J. Richardson, M. Björnmalm, and F. Caruso, "Technology-driven layer-by-layer assembly of nanofilms," *Science*, vol. 348, no. 6233, pp. 2491 1–11, 2015.

[39] C. Processing, *Ceramic Processing*. CRC Press, 2006.

[40] L. E. Scriven, *Physics and Applications of DIP Coating and Spin Coating*, vol. 121. MRS Proceedings, 2011.

[41] J. C. Love, L. A. Estroff, J. K. Kriebel, R. G. Nuzzo, and G. M. Whitesides, "Self-assembled monolayers of thiolates on metals as a form of nanotechnology," *Chemical Reviews*, vol. 105, no. 4, pp. 1103–1169, 2005.

[42] A. D. Becke, "Density-functional thermochemistry. III. The role of exact exchange," *The Journal of Chemical Physics*, vol. 98, no. 7, pp. 5648–5652, 1993.

[43] M. Häser, C. Kölmel, H. Horn, R. Ahlrichs, and M. Bär, "Electronic structure calculations on workstation computers: The program system turbomole," *Chemical Physics Letters*, vol. 162, no. 3, pp. 165–169, 2002.

[44] E. Van Lenthe and E. J. Baerends, "Optimized Slater-type basis sets for the elements 1-118," *Journal of Computational Chemistry*, vol. 24, no. 9, pp. 1142–1156, 2003.

[45] M. M. Francl, W. J. Pietro, W. J. Hehre, J. S. Binkley, M. S. Gordon, D. J. DeFrees, and J. A. Pople, "Self-consistent molecular orbital methods. XXIII. A polarization-type basis set for second-row elements," *The Journal of Chemical Physics*, vol. 77, no. 7, pp. 3654–3665, 1982.

[46] I. A. Salem and M. S. El-Maazawi, "Kinetics and mechanism of color removal of methylene blue with hydrogen peroxide catalyzed by some supported alumina surfaces," *Chemosphere*, vol. 41, no. 8, pp. 1173–1180, 2000.

[47] G. Socrates, *Infrared and Raman characteristic group frequencies. Tables and Charts*. John Wiley and Sons, 2001.

[48] K. L. Killops, M. A. Browe, J. J. Mahle, G. W. Peterson, B. J. Schindler, and J. B. DeCoste, "The effect of water adsorption on the structure of the carboxylate containing metal–organic frameworks Cu-BTC, Mg-MOF-74, and UiO-66," *Journal of Materials Chemistry A*, vol. 1, no. 38, p. 11922, 2013.

[49] N. R. Dhumal, M. P. Singh, J. A. Anderson, J. Kiefer, and H. J. Kim, "Molecular Interactions of a Cu-Based Metal-Organic Framework with a Confined Imidazolium-Based Ionic Liquid: A Combined Density Functional Theory and Experimental Vibrational Spectroscopy Study," *Journal of Physical Chemistry C*, vol. 120, no. 6, pp. 3295–3304, 2016.

[50] A. Abbasi, S. Tarighi, and A. Badiei, "A three-dimensional highly stable cobalt(II) metal-organic framework based on terephthalic acid: Synthesis, crystal structure, thermal and physical properties," *Transition Metal Chemistry*, vol. 37, no. 7, pp. 679–685, 2012.

[51] S. H. M. Wandurraga, *Reduced reaction kinetics model for CO2 dissociation in non-thermal microwave discharges*. PhD thesis, 2015.

[52] D. Y. Lee, I. Lim, C. Y. Shin, S. A. Patil, W. Lee, N. K. Shrestha, J. K. Lee, and S. H. Han, "Facile interfacial charge transfer across hole doped cobalt-based MOFs/TiO2 nano-hybrids making MOFs light harvesting active layers in solar cells," *Journal of Materials Chemistry A*, vol. 3, no. 45, pp. 22669–22676, 2015.

[53] L. G. van de Water, G. L. Bezemer, J. A. Bergwerff, M. Versluijs-Helder, B. M. Weckhuysen, and K. P. de Jong, "Spatially resolved UV-vis microspectroscopy on the preparation of alumina-supported Co Fischer-Tropsch catalysts: Linking activity to Co distribution and speciation," *Journal of Catalysis*, vol. 242, no. 2, pp. 287–298, 2006.

[54] E. Carbonell, B. Ferrer, F. X. Llabrés i Xamena, H. Garcia, and M. Alvaro, "Semiconductor Behavior of a Metal-Organic Framework (MOF)," *Chemistry - A European Journal*, vol. 13, no. 18, pp. 5106–5112, 2007.

Acknowledgements

I would first like to thank my thesis supervisor Guusje Delen for her time and effort in guiding me through my time at the group of Inorganic Chemistry and Catalysis (ICC) of Utrecht University. Whenever I had a question, struggled with my practical work or got stuck in the data analysis, she was always prepared to answer my questions or explain things from a different perspective.
I would like to thank prof. ir. dr. Bert Weckhuysen for giving me the opportunity to do my masters project in his group. With his strict and sometimes funny ways of feedback, I was able to get the best out of myself.
I thank Dr. Florian Meirer as second supervisor for reading and grading my thesis.

A huge thanks goes to Jochem Wijten for measuring the SEM images and assistance in TAS measurements. But the biggest fraction of this gratitude is for the time he spent with me to share his knowledge about all the difficulties I encountered. His patience and well skilled explanatory capacities helped me a lot during my thesis.

I thank Dr. Robert Geitner for this time in performing the DFT calculations. Although it did not seem a lot of work in the beginning, the time he spent on the calculations was significant. All the questions I had were always answered with a smile which makes it nice to work with him.

I thank Laurens Mandemaker for his time in discussing with me IR and MOF related subjects. The discussions lead to a better understanding of my data. Furthermore, I would like to thank him for the ToF SIMS measurements and assistance with AFM measurements.

A great smile goes to my friends and study colleagues Thimo Jacobs and Jeroen Dubbeld. Their presence during the time I wrote my thesis made my days joyful. They were always open for discussions or a casual talk with a cup of coffee.

I thank Arie Bleij for his cooking every Tuesday. I was able to work some more hours in the evening and got a good meal afterwards.

I thank my brother Nijs Bouman for designing the beautiful cover page.

The lunch breaks were always nice in the presence of my master colleagues and friends: Albaraa, Andries, Angela, Dónal, Claudia, Guido, Jelle, Kris, Liselotte, Matt, Onno, Oscar, Peter, Stefan, Tessa, Willem and Wolfer.

Appendices

Appendix 1

Theory on TAS measurements

When light is irradiated on matter, the light can be absorbed. For photo-active compounds, the energy of the light can be used to induce exciton formation. Electrons are elevated from the ground state to excited states. This create a electron in a high energy state leaving a positively charged hole in the ground state. With time, these two charge carriers will relax back to the ground states. With transient absorption spectroscopy (TAS), the half-life times of excitons in materials can be measured, see Figure 11.36.

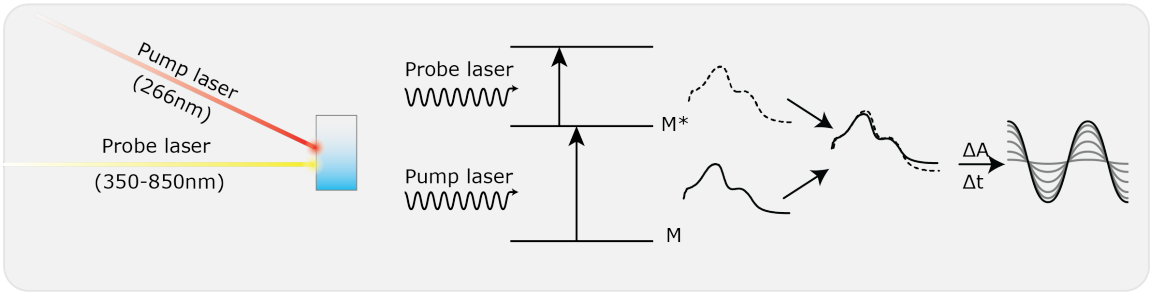

Figure 11.36: Schematic illustration of transient absorption spectroscopy (TAS). A pump laser excites the sample. The probe laser measures the absorbance over a certain Δt. The difference in absorbance between the excited and the non-excited materials signal is plotted over the time. Half-life times of the excited states can be obtained via mathematical polynomials that fit the observed excitation decays.

The measurement in TAS requires two lasers: a pump laser and a probe laser. The pump laser excites the material. The probe laser probes the absorbance after excitation. After the laser pump, a fraction of the material is excited. With time this fraction of excited material decreases and relaxes back to the ground state. During this time, the probe laser measures the absorbance. First, it measures the absorbance of the non-excited material. After that, the probe laser measures at different times (after the pump laser) the absorbance of the excited material. With increasing time, the fraction of excited species will decrease. The output of the TAS data will be the difference in the absorbance state of the non-excited material and the excite state of the material: ΔA. This means that right after the pump laser, there will be relatively a lot of species be excited, resulting in a large ΔA. After a while, the fraction of excited species is reduced, and a smaller ΔA will be observed. The pump laser is pulsed. This creates a time domain. Measurement on the decay of the excited material can be measured in the time between the pulses. For example, if the pulse is set on 10 hertz, the pump laser excites the material every 100ms. The time scale of the measurements is than 100ms. Within this time, the probe laser has to measure the absorbance of the excited material. Over a longer time, (minutes and hours), the measurements create a distribution of different ΔA at different times. The higher the overall measuring time, the better the measurement resolution will be.

Appendix 2

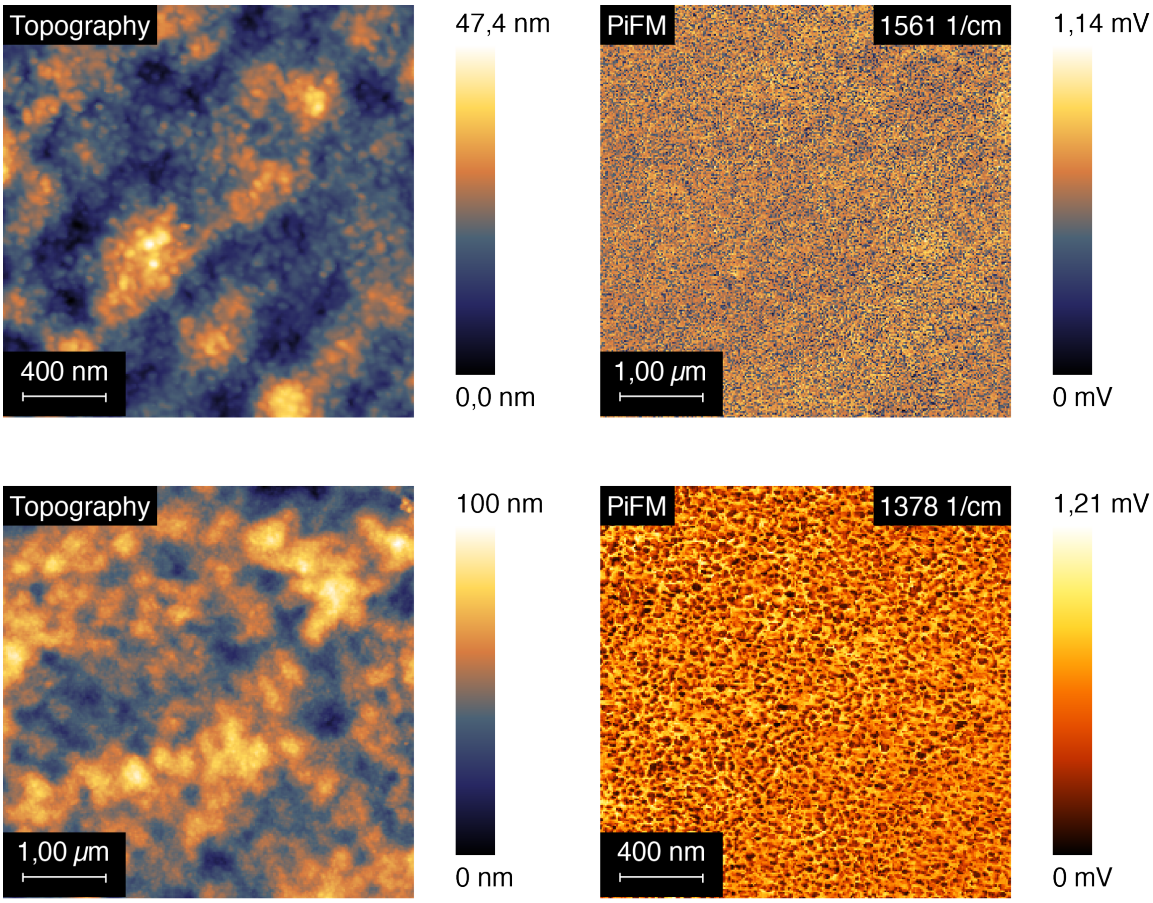

Figure 11.37: AMF-IR results of CoATA@Au. Chemical mapping at 1561 and 1378 cm^{-1} demonstrate a chemically homogeneous coating of CoATA.

Appendix 3

During the practical work on this thesis, experiments on a multivariate MOF thin film had been performed. For this MOF thin film, amino terepthalic acid (ATA), mono-hydroxide terephthalic acid (MHDA) and 4,4'-bipyridine (44BP) were dissolved in ethanol and with layer by layer synthesis (LbL), films were obtained. The LbL program was:

$CoCl_2 \cdot 6\ H_2O$	1mM	1 min
EtOH	150 rpm	10 sec
MHTA, DHTA, 44BP	0.8, 0.8, 0.4mM	4 min
EtOH	150 rpm	10 sec

XRD measurements did not show any crystalline product but with ToF SIMS, some interesting chemical mapping was obtained. In figure 11.38 the results are shown.

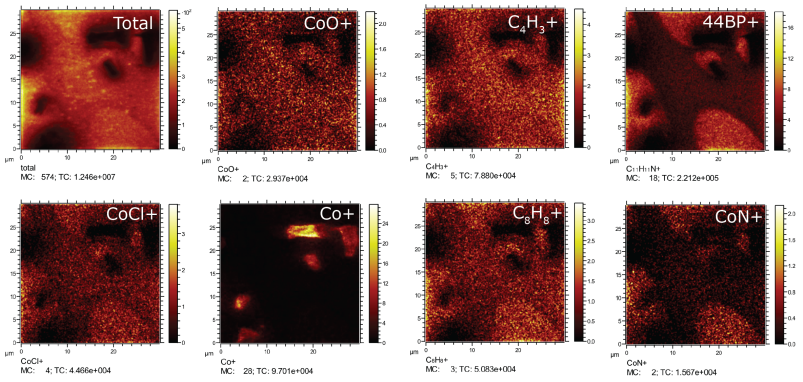

Figure 11.38: ToF SIMS results of a cobalt with ATA, MHTA and 44BP thin film.

In the figure we see that the $C_{11}H_{11}N^+$ and CoN^+ fractions nicely correlate but are not homogeneously distributed over the surface. Next to that, the $C_4H_3{}^+$ (arising from the terephthalic derivatives) and the CoO^+ do correlate too. The bibyridine fractions and terephthalic fraction, however, are not really correlated. The 'finger-like' print on the right bottom part of the images consists mostly out of Co44BP. The terephthalic acid derivatives appear somehow randomly over the surface and do not correlate significantly with any cobalt species. There is no explanation yet why, at the right top corner, cobalt species are accumulated. There is no chloride present, clustering of the precursor ($CoCl_2$) was not taken place.

Appendix 4

During this project, the construction of a photovoltaic cell with a MOF was carried out. The construction of such a device could be good for the analysis on both the light harvesting properties and catalytic possibilities but also on the determination of the LMCT / bandgap position vs SHE.'. This type of solar cell originates from a dye sensitized solar cell (DSSC). In this type of device, a light harvesting materials is covalently bonded to a (mesoporous) titania surface. The titania is pasted on FTO glass. The solar cell is finished by placing FTO class on top of the cell and a electrolyte solution is added in between. The surface of the FTO class should contain a thin layer of graphene / platinum. A common electrolyte solution is based on the redox couple I_2/I^-. The Pt/graphene act as catalyst for the reaction of I_2 to I^-. When light hits the surface of the dye@TiO_2, the dye is excited. The electron transports to the conduction band of the titania. Via the FTO glass the electron can provide work. On the top part of the device electrons are collected by the I_2. The hole of the dye is then finally scavenged by the I^-.

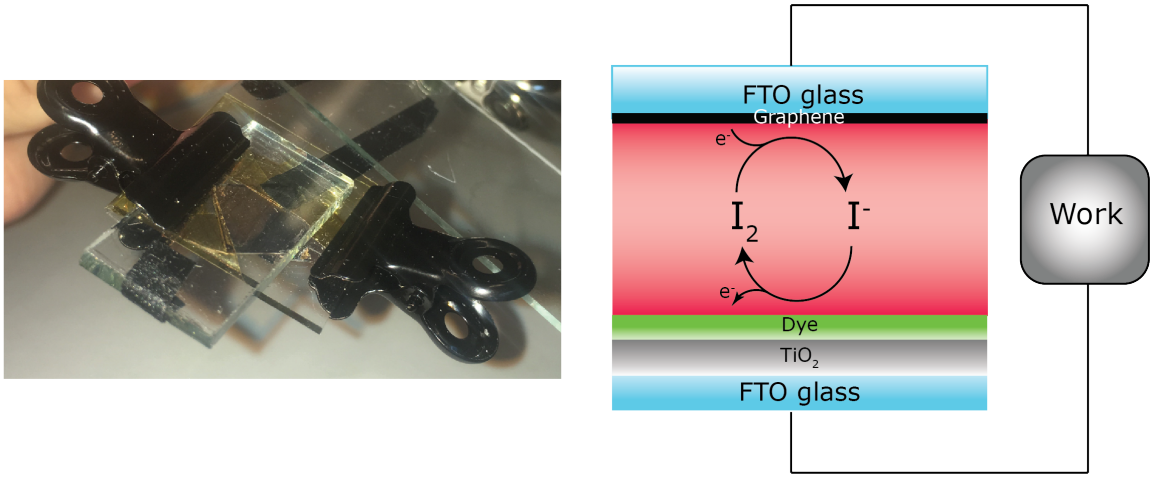

Figure 11.39: Left: A picture of the first crafts for a MOF sensitized solar cell. Right: schematic illustration of a dye sensitized solar cell.

For the MOF sensitized solar cell (MSSC), CoDHTA was first used as the semiconductor material (replacing titania). A voltage was measured but was not stable. It could not been determined if the potential was induced by the open circuit voltage or the destruction of the MOF film.
To investigate the light harvesting and electron transport performance, CoDHTA was subsequently used as dye on top of a mesoporous titania layer. The titania coating on the FTO class was prepared using a sol-gel solution of titania isopropoxide and spin coated on the substrate. The CoDHTA was spin coated as described in the methodology section. The sample was called CoDHTA@TiO_2@FTO. The device was crafted by placing the CoDHTA@TiO_2@FTO on a FTO glass (3x3cm) coated with a graphite pencil. Teflon tape was used to make sure the two FTO glass substrates did not make contact with each other. A solution of iodine (57mg) and potassium iodide (162mg) was prepared in 20mL ethanol. This solution was 10x diluted. The two FTO substrates were kept in place using a binder clip. The FTO substrates were place in a way so a small fraction of the class was free so an electronic

crocodile beak could be attached, see figure 11.39.
The MSSC project stagnate at a certain moment because the lab did not provide a proper setup for accurate measurements on the potential / current measurements. The difference between a MSSC with and without MOF was difficult to determine because is was very difficult / impossible to reproduce the exact measurement. Under exposure of light, a current up to 20μA was observed for both MSSC with and without MOF.